



OPEN

Interplay of tectonic and dynamic processes shaping multilayer extensional system in southern-central Apennines

Rita de Nardis^{1,2}✉, Alessandro Vuan^{3,4}, Luca Carbone^{1,2}, Donato Talone^{1,2}, Maria Adelaide Romano³ & Giusy Lavecchia^{1,2}

High-hazard seismic zones can remain silent over centuries with meager seismicity rates challenging our understanding of seismic processes. We focus on the comprehensive analysis of cascading episodes of swarms and seismic sequences following the 2009 L'Aquila mainshock (M_w 6.3) in the southern-central Apennine that previously experienced ~ M7 earthquakes. We enhance the seismic catalog, unmasking low-magnitude seismicity down to completeness magnitude $M_L \sim 0$, and we unveil that the microseismicity might be secondarily triggered by the L'Aquila mainshock, influencing the frictional properties in the nearby fault zones or opening fault valves generating the intense seismic activity detected from 2009 to 2013. The diffusivity, observed in the most seismic episodes, and the high V_p/V_s values (> 1.88) indicate fluid circulation promoting multilayered extensional seismicity within 11–15 km and 16–23 km depth ranges. Mapping the 3D distribution of seismicity alongside geological data reveals an evident tectonic influence, unveiling unknown geometric aspects and providing the first evidence of a NNE-dipping deformation zone bounding at depths of 11–15 km the overlying fault system. Deeper seismicity suggests a mantellic CO_2 ascending shape. These findings enrich the literature on tectonic seismic swarms in extensional domains, providing essential constraints on fluid involvement in the seismic processes and contributing to forthcoming discussions on the seismotectonic setting in high-seismic-risk areas of the Apennines of Italy.

Keywords Triggering, Swarms, Seismic sequences, 3D fault models, Southern-central Apennines, Italy

After a significant seismic event, the regional earthquake rate increases for days, months, or years¹ over a distance comparable with the dimension of the source (aftershocks), or much further (up to thousands of kilometers) with fault failure implications on active structures critically stressed^{1–4}. Hence, large earthquakes can trigger microseismicity or slow-slip events from intermediate to long distances depending on the local stress state and the size of the stress perturbation, which can broadly range from ~ 0.1 kPa to ~ 1MPa⁵. Triggered microseismicity has been well documented since the Landers earthquake (1992, M_w 7.3) in correspondence to geothermal and volcanic sites and tectonically active areas mainly occurring at the edges of locked faults and deep basins⁶.

Remote earthquake triggering can directly depend on passing surface waves inducing deformation on fault zones, indirectly acting on frictional properties, or unlocking a fault by opening a fluid pressure valve^{2,7–11}. On the other hand, the observations of these phenomena at large distances open the question of whether there is a direct connection between the main triggering event and observed seismic activity when earthquakes are delayed in time^{5,12}. Dealing with delayed-dynamic triggering processes, it is frequently challenging to establish a conclusive argument that attributes the triggering solely to the transient dynamic wavefield.

It is well known that space-time earthquake clustering, observed in volcanic and active tectonic areas, can be favored by the seismic and aseismic transient local processes as fluid flow, fault creeps, or magma intrusion¹³. Moreover, in active tectonic areas, clustering can also be linked to slow slip events^{14,15} and show specific characteristics in durations (days, weeks, months), moment release (delayed from the onset of the clustering activity), and migration velocities (from 1 km/h to 1 km/day).

¹University of Chieti-Pescara, via dei Vestini 31, 66100 Chieti, Italy. ²CRUST - Centro interUniversitario per l'analisi SismoTettonica tridimensionale, Chieti, Italy. ³National Institute of Oceanography and Applied Geophysics – OGS, Trieste, Italy. ⁴Istituto Nazionale di Geofisica e Vulcanologia, INGV – Centro Nazionale Terremoti, Roma, Italy. ✉email: rita.denardis@unich.it

Understanding the physical processes underlying seismicity clustering, triggered after major earthquakes or other phenomena, is of fundamental importance for improving the knowledge on the stress redistribution required for fault failure and the degree of clock advances earthquakes in high seismic hazard areas.

This paper focuses on the seismicity following the 2009 L'Aquila earthquake (M_w 6.3) in the southern sector of the central Apennines, a high-seismic-risk region undergoing tectonic extension (Fig. 1a).

Southward of the causative fault of the L'Aquila 2009 main event (e.g., Paganica fault), a general increase of the seismicity rate at some fault lengths (~ 60 km) is observed close to Sora town (grey rectangle Fig. 1b,c). This area is characterized by a low level of background seismicity that has increased fivefold from 2009 to 2013 (Fig. 1d) with cascading episodes of seismic clustering at an average depth of ~ 11 – 14 km that climaxed with deeper events on 16th of February 2013 ($M_w^{\max} \sim 5$, QRCMT¹⁶) at a depth of ~ 17 – 20 km¹⁷. The mainshock of the 2013 seismic activity represents the most energetic event of the last ~ 100 years (Fig. S1).

These episodes of seismic sequences and swarms occurring after the L'Aquila earthquake at different seismogenic depths raise questions about the remote triggering, the role of fluids, the tectonic control, and the thickness of the seismogenic layer of the extensional domain.

The primary objective of this paper is to elucidate the significance of the increase in seismicity and to gain insights into the genesis of the observed clusters of earthquakes. This is achieved by investigating the space-time evolution of the intense seismic activity, characterizing each seismic episode in terms of migration velocity and V_p/V_s ratio, and exploring the potential correlation of event distribution with local tectonic factors, including pre-existing fault geometry and kinematics influencing the multi-depth earthquake nucleation and distribution.

Furthermore, seismological analyses are conducted to study the swarms and the evolution of the Sora seismic sequence, aiming to define the relationships between the occurrence of the observed seismic activity and the distribution of static and dynamic stress transfer induced by the L'Aquila earthquake, as well as transient (e.g., fluid involvement) or tectonic phenomena.

Seismotectonic framework

Central Apennines in Italy is a high-seismic-risk area undergoing extensional tectonics (Fig. 1a) stretching at low rates of 3–4 mm/yr in the SW–NE direction^{27,28}. This extensional belt is characterized by NNW–SSE to WNW–ESE striking normal to normal-oblique faults, Late Pliocene to Quaternary in age²⁵. The overall system is composed of high-angle westward-dipping segments detaching on eastward-dipping low-angle basal planes^{29–32}. The seismicity associated with this framework is mainly located at upper crustal depths (< 12 – 14 km)¹⁷ and is primarily controlled by tectonic processes. Locally, deeper normal events are observed along the extensional domain, such as the Matese seismic sequence of December 2013–January 2014 (M_w 5.2, QRCMT¹⁶), that occurred at depths ranging from 10 to 25 km^{33–35} (Figs. 1a and S1a). The hypothesis of associating these deeper events with intrusive episodes of magmatic sources has been advanced by Di Luccio et al.³⁶.

The focal mechanisms of the major earthquakes, including those of the deepest events, show an SW–NE trending nearly horizontal T-axes, also consistent with the long-term Quaternary stress field^{18,20,34} (Fig. 1a and S1a).

The area, affected by the increasing seismic activity after the L'Aquila 2009 earthquake, is in correspondence with inner fault alignments of the Apennines extensional domain³⁷ (Figs. 1b,c and S1).

The seismic catalogs^{22,23} report that the southern-central Apennines experienced four significant events during the last ~ 700 years: the 1349 earthquake (Io X MCS, M_w 6.8), 1654 (Io IX–X MCS, M_w 6.3), 1915 (Io X–XI MCS, M_w 7.1) and 1984 one (Io VIII MCS, M_w 5.8) (Figs. 1b, S1b and S2a–c).

The Fucino–Marsicano–Barrea alignment (Fig. 1b) is highly seismogenic. The Fucino segment has been associated with the large and devastating earthquake in 1915 (M_w 7.1), while the Barrea segment with the 1984 seismic event (M_w 5.8)³⁸. The latter was of lesser magnitude but also destructive. A consensus exists in the literature on the seismogenic behavior of this alignment and the individual seismic sources of these two earthquakes (Figs. 1b and S1b).

On the contrary, the Villavallelonga–Pescasseroli–San Donato Val Comino, the Balsorano–Posta Fibreno, and the Sora faults are still debated segments (Figs. 1b,c, and S1b). They represent faults mapped at the outcrop scale with well-exposed fault planes^{25,26,39–43}, with few associated seismicity.

The source of the 1654 earthquake (Fig. S2a,b), reviewed by⁴⁴ using the macroseismic field and coseismic effects, is associated with the Sora fault (Fig. 1b).

Finally, the 1349 event was a significant earthquake in a portion of the extensional domain considered a seismic gap by⁴⁵ due to the significant moment release deficit in the last 500 years (Fig. S2a–c).

The study area (grey rectangle in Figs. 1b,c, and 2) is bordered eastward by the Fucino–Marsicano–Barrea SW-dipping alignment. It is crosscut by SW to WSW-dipping normal fault systems of Villavallelonga–Pescasseroli–San Donato Val Comino, as well as by the innermost right-stepping en-echelon Balsorano–Posta Fibreno sets and Sora fault. Westward, it is bound by the southern termination of Ernici NE to NNE-dipping fault systems. Over time, the area has experienced several moderate events with magnitude around M 5–5.5 that occurred in the study area (1693, M_w 5.2; 1771, M_w 5.1; 1873, M_w 5.4; 1874, M_w 5.5; 1877, M_w 5.2; 1901, M_w 5.1; 1922, M_w 5.2; 1927, M_w 5.2 (Fig. S1b)^{22,26}.

In contrast, a low level of seismicity rate characterizes the study area. A great effort to highlight the minor seismicity was made by experiments performed through temporary seismic networks^{46,47} and recently by⁴⁸ that relocated the seismicity from 2009 to 2013 and computed a rich dataset of low-magnitude events and focal mechanisms ($0 \leq M_L \leq 4.8$). The genesis of seismic events occurring in this internal sector of the Apennine's extensional domain is still debated. In fact, in addition to tectonic loading, the presence of higher CO_2 and heat flux values compared to the external sectors^{49,50} suggests that overpressurized CO_2 reservoirs at upper crustal depths may contribute to seismicity in the study area.

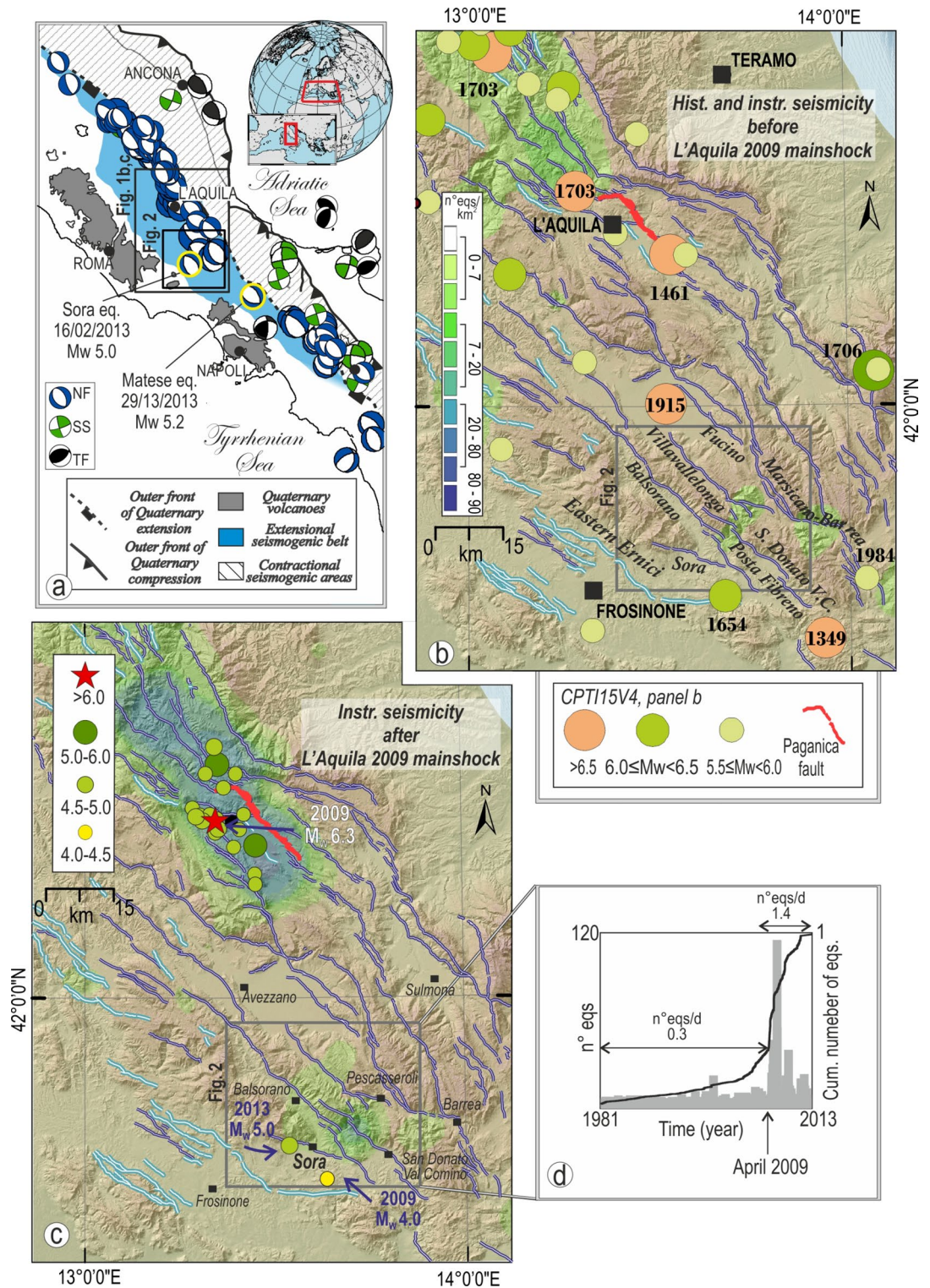


Figure 1. Instrumental and historical seismicity in the southern-central Italy tectonic framework (ArcMap, by ESRI, ArcMap/ArcGIS, v. 10.8, <https://www.esri.com/en-us/home>). (a) Extensional and contractional domains in southern-central Italy¹⁸ and major focal mechanisms ($M_w > 4.5$) from^{19,20}. (b) The density contour of the instrumental seismicity distribution ($0 \leq M \leq 5.8$) from 1981 to March 2009²¹ and main seismic historical and instrumental events ($M_w \geq 5.5$) occurred in the study area before the L'Aquila seismic sequence (colored symbols as in the legend)^{22,23}. The active fault patterns are from the QUIN database^{24,25} integrated with details from the geological map of Italy (scale 1:100.000 and 1:50.000) and from²⁶. Blue lines represent the west-dipping normal faults, and the light blue colors show the northeast-dipping ones. (c) Density contour of seismicity distribution ($0 \leq M \leq 6.3$) and main seismic events that occurred in the study area after the L'Aquila seismic sequence (from 2009 to 2020). The magnitude of the Sora seismic event is from QRCMT¹⁶. (d) Histogram summarizing the frequency of instrumental seismicity before and after the L'Aquila seismic sequence in the study area (grey rectangle in panels b and c).

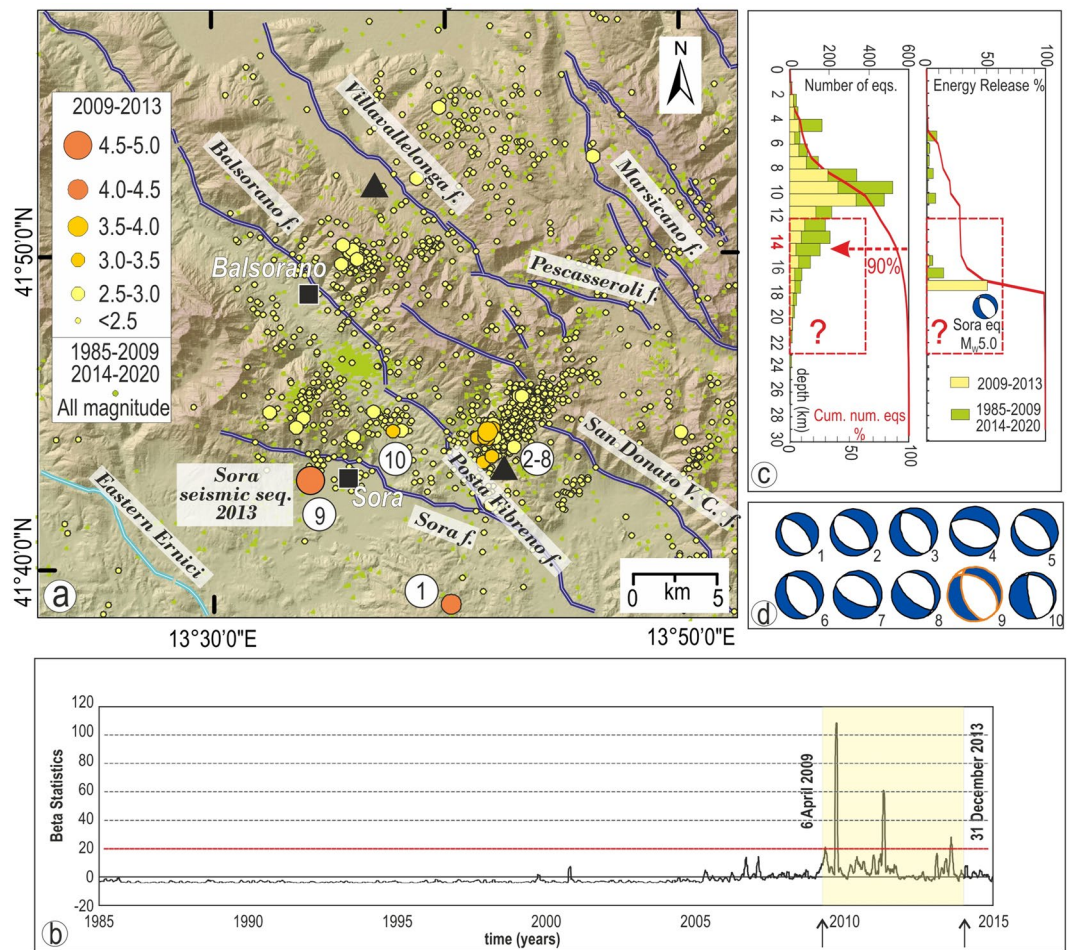


Figure 2. The main characteristics of instrumental seismicity occurred in the study area from 1985 to 2020 ($0 \leq M_L \leq 4.8$) as reported in the Italian Seismic Bulletin²¹. (a) Map distribution of seismic events (ArcMap, by ESRI, ArcMap/ArcGIS, v. 10.8, <https://www.esri.com/en-us/home>; ESRI, 2021). Light green dots represent earthquakes before 2009 and after 2013, while yellow-orange dots are the analyzed events. White circles with numbers from 1 to 10 refer to the focal mechanisms represented in panel (d). The black triangles represent two of the 7 permanent seismic stations used for enhancing the catalog. The complete configuration is shown in Fig. S3. (b) Beta Statistics computed for the study area since 1985 using a bin of 30 days and non-overlapping windows. (c) Depth distribution of earthquakes and the corresponding energy release. (d) Focal mechanisms of seismic events with $M_L \geq 3.0$ from⁴⁸. The orange-bordered focal mechanism is related to the Sora earthquake.

Data and material

To perform a spatial-temporal analysis of the seismicity within the study area, we built a new seismic catalog having ~17,800 seismic events ($-1.3 \leq M_L \leq 4.8$) that occurred from 2009 to 2013 between the Fucino-Marsicano-Barrea SW-dipping alignment and the Ernici NE-NNE dipping fault systems (Figs. 1a and 2a). The enhanced seismic catalog was retrieved by using a template matching technique considering as templates the 856 relocated events of the Catalog of Absolute (nonlinear) 3D earthquake Locations^{17,51} with horizontal errors < 3 km and vertical errors < 4 km (Fig. 3).

We collected the focal mechanism solutions of the events that occurred in the same time interval (2009 to 2013) from the relevant literature^{19,20,48}.

Finally, the results of our analysis were opportunely integrated with geological information on active faults^{24–26,43} and the CO₂ emissions⁵⁰.

Results

General characteristics of instrumental seismicity

From 1985 to 2009, before the 6th of April L'Aquila mainshock (M_W 6.3), the study area is characterized by a meager rate and sparse seismicity (~0.3 events/day) (Figs. 1c,d, and 2). After the L'Aquila mainshock, the activity rate increased five times up to the end of 2013. Such seismicity was characterized by about one thousand seismic events with $M_L < 4.0$, except for the Sora earthquake (M_W 5.0) that occurred on the 16th of February 2013.

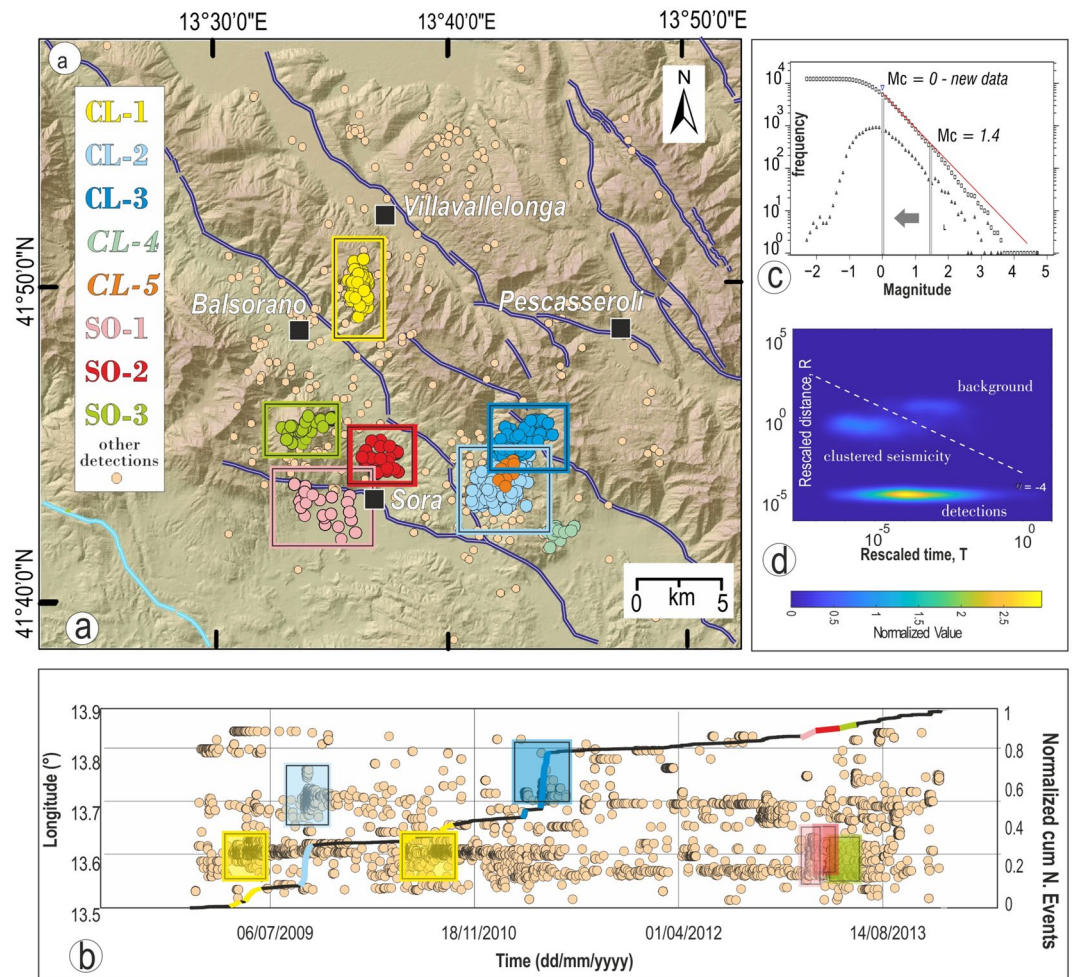


Figure 3. Main characteristics of the enhanced catalog. **(a)** Map showing the new catalog obtained using template matching technique and the spatial distribution of the main clusters CL-1-CL-3 and SO-1-SO-3 and minor clusters CL-4, CL-5 (ArcMap, by ESRI, ArcMap/ArcGIS, v. 10.8, <https://www.esri.com/en-us/home>; ESRI, 2021). **(b)** Temporal evolution of the analyzed seismicity for longitude. The colored rectangles indicate the clusters CL-1-CL-3 and SO-1-SO-3. **(c)** Gutenberg-Richter slope evaluated with the new catalog. The grey bars mark the completeness magnitude (M_c) of the old and new datasets. **(d)** Distribution of the nearest-neighbor distance for the analyzed seismic events computed with⁶⁰ code. The plot displays the joint distribution of the re-scaled time and space components (T, R). Spatial and temporal occurrence of the analyzed seismic events.

This sharp temporary increase affects the study area with seismicity spatially distributed with well-identifiable localized clusters (Figs. 2 and 3).

The beta statistics analysis of the seismicity, which quantifies the seismicity rate changes⁵² (Fig. 2b), shows two increases in seismicity rates: one after 2005 and the other after 2009. The first variation is due to an improvement of the Italian National Seismic Network (Rete Sismica Nazionale, RSN)⁵³ that produced a better-quality earthquake detection capability and lowered the earthquake catalog completeness threshold. The second one, and it is composed of at least four evident anomalies exceeding the average background rate by more than 20 standard deviations after the 6th of April 2009. Such anomalies were never observed before in the study area.

The frequency–depth histogram of the instrumental seismicity (1985–2020) depicts a bimodal pattern with maxima centered around 10 km and 14 km depths. Although the two peaks cannot be properly distinguished within the depth formal errors, this bimodal shape is widely observed along the Apennine chain in areas with outcropping normal faults and regional low-angle antithetic normal faults or basal detachments^{54–57}. It is important to emphasize that, in this region, the base of the seismogenic layer deepens compared to observations in the central Apennines and is similar to those in southern Italy (e.g.,^{58,59}). About 90% of the events occur at depths less than ~14 km, while the remaining 10% occur at the lower crust depths (17–20 km). In the observed time interval, from an energy release point of view, we can see that the deepest events below the base of the seismogenic layer can have magnitudes comparable to or greater than the shallower ones (Fig. 2c).

The focal mechanisms of the minor events and the deep Sora earthquake show SSW–NNE to SW–NE T-trending axes compatible with the tectonic stress acting in the study area (Figs. 1a and 2d).

The new 2009–2013 seismic catalog

The waveform-based template matching technique allows us to augment the seismic catalog and enhance seismicity's spatiotemporal evolution (Figs. 3 and S4).

Starting from ~ 856 templates, we obtain a significant increment of the output catalog of ~ 21 times (Fig. 3a,b). The new catalog comprises ~ 17,800 seismic events ($-1.3 \leq M_L \leq 4.8$) that occurred from 2009 to the end of 2013, containing multiplets and quasi-repeating events (Figs. 3b and S4). Figure 3b shows the newly detected earthquakes clustered multiple times. The high number of detections suggests the sensitivity of the template matching to multiple repeating over time seismic processes.

The enhanced catalog significantly improved the completeness magnitude, lowering M_c from 1.4 to 0 (Fig. 3c) and filling temporal gaps between the occurrence of larger ones.

The Zaliapin et al.⁶⁰ declustering method applied to our catalog clearly shows that the distribution of time and space components (T, R) of the nearest-neighbor distance follows a prominently trimodal pattern, revealing the existence of three statistically distinct earthquake populations (background, clustered seismicity, multiplets and quasi-repeaters (Figs. 3d and S5). The results from the combination of waveform clustering are summarized in Figs. 3 and S4. This type of pattern is always observed when new detections are co-located with their templates, as discussed in⁶¹ (see Method section).

This approach allows us to separate background and clustered seismicity and highlights with different behaviors, foreshocks-mainshock-aftershock (FMA), and swarms or swarm-like sequences (S). We identify 8 clusters and deeply analyze six relevant episodes for a) duration, b) the number of earthquakes, and c) magnitudes. We call them CL-1-5 and SO-1-3 (Fig. 3). They are in three well-distinct epicentral positions: (1) south of the Villalonga locality (CL-1), (2) southward of Pescasseroli (CL-2 and CL-3 and two minor clusters CL-4 and CL-5) and (3) in the proximity of the Sora town (SO-1, SO-2, SO-3).

Temporal behavior

Starting from the enhanced catalog and its declustering, we could identify eight clusters from 2009 to 2013 in distinct space and time intervals, showing a complex temporal behavior (Fig. 3, Table S1).

CL-1 is the northernmost cluster that occurred on the 7th of April 2009, 34 h after the LAquila mainshock (M_W 6.3). It comprises 2332 earthquakes, and its temporal activity is highly variable up to May 2012 (Fig. S5). The seismicity shows an intermittent behavior evolving in four main phases during 2009–2010 and nearly occupying the same volume (Fig. 3). The maximum magnitude of each phase ranges from 2.6 to 2.7, and their duration is dozens of days (12–64 days). Following⁶² classification, the cluster can be considered as foreshock-mainshock-aftershock (FMA) and pure swarm (S) behavior alternately during the four phases (Fig. 4a–d). Figure 4 clearly illustrates that microseismic sequences (CL-1, I-Phase, and III-Phase) characterized by prominent mainshocks are succeeded by more prolonged swarm activity involving approximately one thousand seismic events (CL-1, II-Phase, and IV-Phase).

The coefficient of variation of interevent times (COV in Fig. 4a'–d'), representing the degree of clustering between consecutive seismic events, shows higher values corresponding to the occurrence of the most energetic events, consistently with what has been observed through the cumulative events over time (Fig. S6a), the COV trends are variable. During the first and third phases, they indicate higher temporal clustering at the beginning of the seismic episode. The second and the fourth phases are relatively constant, suggesting a steady pattern of seismic activity. On the contrary, the maximum-to-cumulative moment ratio (MMR in Fig. 4a''–d'') shows a simple trend for the first and third phases, with maximum values occurring at the beginning of the seismic activity in correspondence with the maximum magnitude while the second and the fourth phases show a complex pattern consistently with the magnitude distribution of the seismic episodes.

CL-2 and CL-3 mainly occurred in October 2009 and May 2011 (Figs. 3a and 4e,f). They appear to form a unique cluster but, they are well separated at depth, as described in section "3D tectonic control in seismic sequence evolution".

CL-2 and CL-3 are composed of two phases that are difficult to separate over time. For this reason, in the text, we simply refer to CL-2 and CL-3. They exhibit a less complex temporal behavior than CL-1 (Figs. S5b and S6b) and comprise thousands of seismic events (~ 4000 and ~ 5000, respectively) with a maximum magnitude of M_L 3.6 and 2.8, respectively. CL-2, overall, can be considered a swarm similar to CL-3⁶². CL-2 coefficient variation of interevent times displays a distinct peak corresponding to higher magnitudes (Fig. 4e',f'), showing a very high clustering of events with COV ~ 6. CL-3 shows low values over time (COV < 2). CL-2 and CL-3 maximum-to-cumulative moment ratios reveal complex patterns, with MMR reaching values beyond 0.75 (Fig. 4e'',f').

Unlike CL-1-CL3, SO-1-SO-2 occurred at deeper layers, occupying different volumes. The seismogenic depth boundary (Fig. S7) and the map distribution of epicenters (Fig. 3a) clearly show that, although partially temporal overlapping (Figs. 5a–c and S5c), SO-1-SO-3 cannot be considered a unique cluster, but three different seismic episodes.

SO-1 is a foreshock-mainshock-aftershock (FMA) seismic sequence with a prominent mainshock (M_L 4.8) occurring at ~ 17 km. The enhanced catalog contains 30 seismic events before the mainshock and allowed us to detail the foreshock sequence, highlighting a pre-seismic quiescence of approximately 13 h. Except for the main event, all the other earthquakes have a magnitude less than ~ M_L 2. The coefficient of variation of interevent time shows high variability only in correspondence with the mainshock and low values for the remaining part of the sequence (Fig. 5a–a'').

SO-2 is located a few kilometers northeast of SO-1 and can also be considered a FMA seismic sequence. The main event (M_L 3.2) occurred on the 23rd of February 2013, but it started on the 17th of February, only one day after the M_L 4.8 earthquake. Similar to SO-1, the coefficient of variation of interevent time is higher in

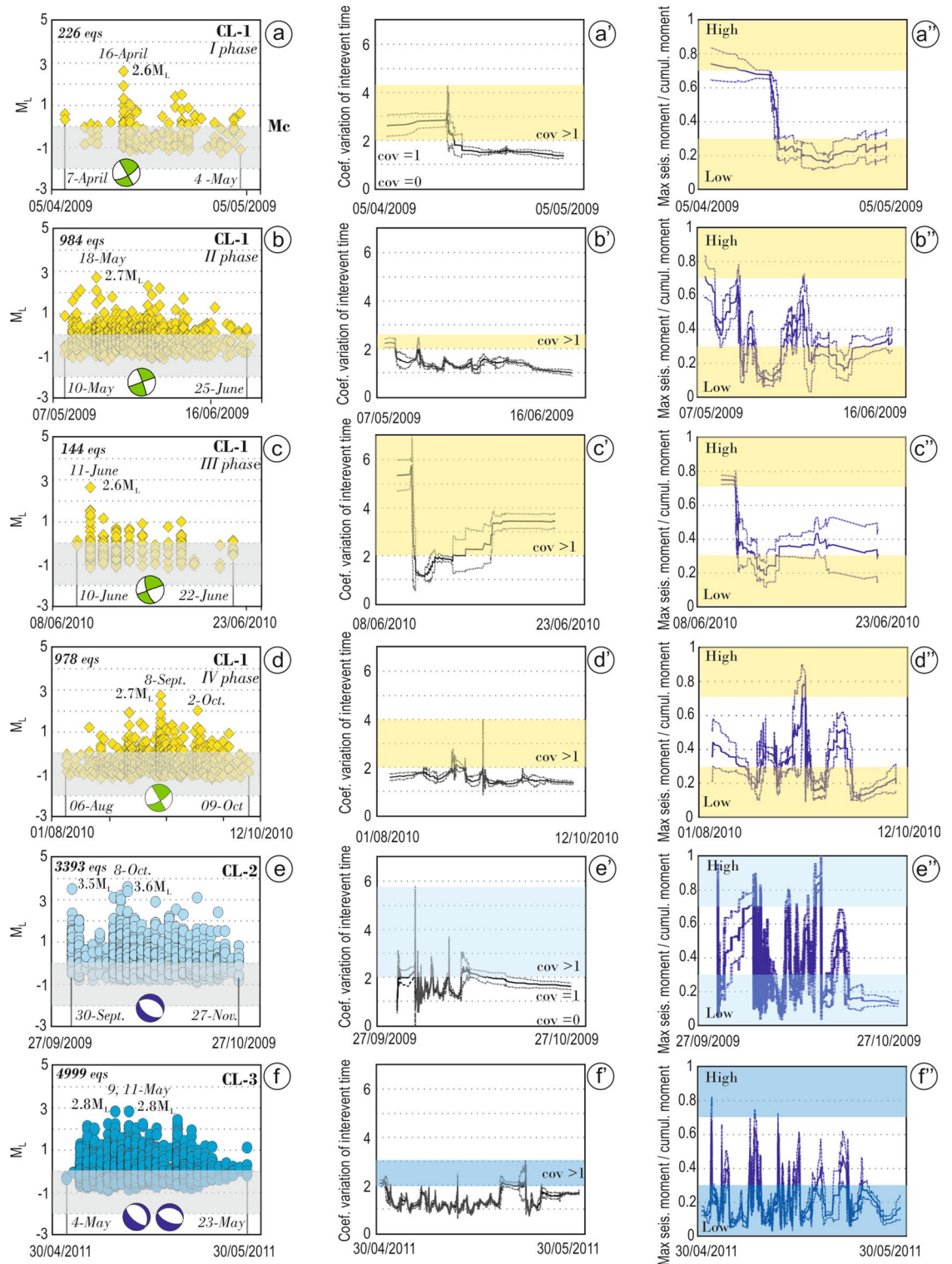


Figure 4. General characteristics of CL-1-CL-3 clusters. (a–f) Magnitude vs time distribution. The grey bands represent the completeness magnitude threshold ($M_c=0$ in Fig. 3). (a’–f’) Coefficient variation of interevent times (COV). The colored bands indicate the degree of COV variation (thin band=low variation, thick band=high variation). (a’’–f’’) Maximum seismic moment, cumulative seismic moment ratio (MMR). Similar to COV, the colored bands highlight low (MMR<0.25) and high (MMR>0.75) MMR values.

correspondence with the main event, and after that, it shows a quasi-flat trend (Fig. 5b’). The moment ratio trend is more complex due to some aftershocks with a magnitude of $\sim M_L$ 3.0 (Fig. 5b’’).

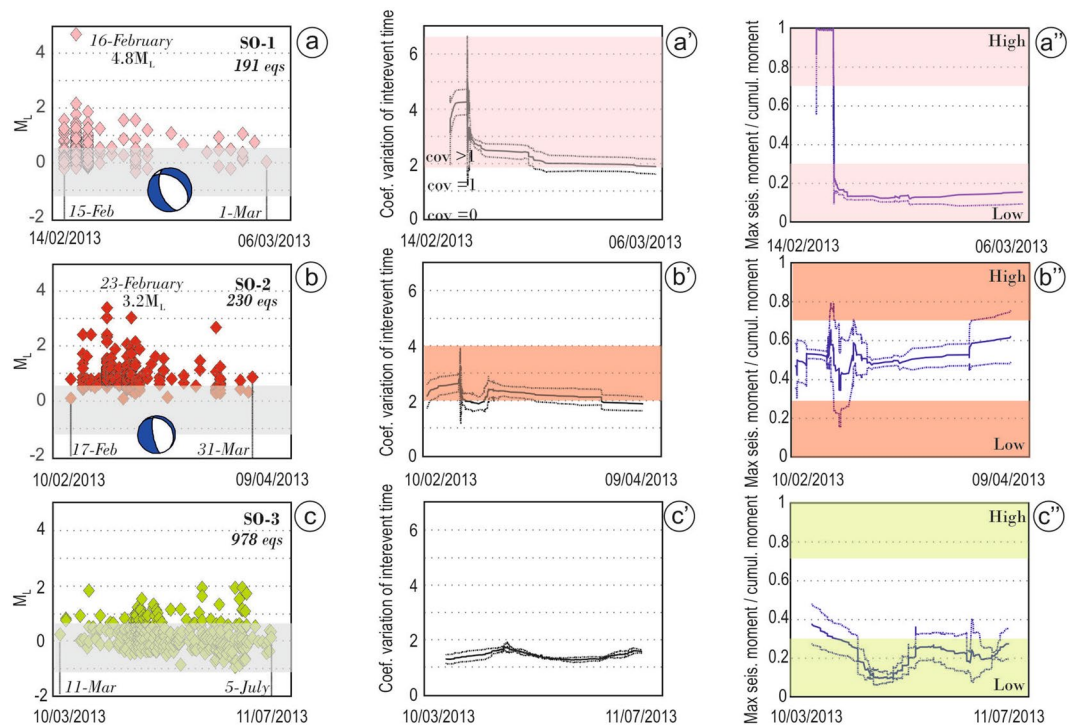


Figure 5. General characteristics of SO-1-SO-3 clusters. (a–c) Magnitude vs time distribution. (a’–c’). The grey bands represent the completeness magnitude threshold ($M_c = 0$ in Fig. 3). Coefficient variation of interevent times (COV). The colored bands indicate the degree of COV variation (thin band = low variation, thick band = high variation). (a’’–c’’) Maximum seismic moment, cumulative seismic moment ratio (MMR). Similar to COV, the colored bands highlight low ($MMR < 0.25$) and high ($MMR > 0.75$) MMR values.

SO-3 is located a few kilometers north of SO-1. It started in March 2013 and temporally overlapped with SO-2. The coefficient variation of interevent and the maximum-to-cumulative moment ratio time history of SO-3 do not show relevant trends with low values of COV and MMR (Fig. 5c–c’). The magnitude, COV, and MMR over time for all spatial clusters are represented in Fig. S5. The main parameters characterizing the identified clusters are summarized in Table S1.

Migration velocity, diffusivity, and V_p/V_s main characteristics

The four seismic phases of CL-1, classifiable as FMA, S, FMA, and S, migrate at an average velocity of 0.2–1 km/d, extending in an area of ~4 km (along strike) by ~2 km (along dip). The volume occupied by all CL-1 phases is the same. At the same time, the temporal evolution of CL-1 is not uniform (Phase I–IV in Figs. 4a–d and S6a), indicating that the architecture of the fault zone and the strength of heterogeneities is variable⁶³.

For each cluster, we set the first event as a reference point, and we compute the distance of all the hypocentral locations to it. This allows us to observe, that the migration patterns of most of the analyzed seismicity grow monotonically with the square root of time according to the⁶⁴ theoretical curve, thus suggesting that the seismicity might be driven by pore-pressure diffusion (Fig. 6). The retrieved hydraulic diffusivity D varies from 0.4 to 1.5 m^2/s during the four seismic phases. The V_p/V_s ratio shows values ranging from 1.88 to 1.92 (Fig. 7), suggesting fluid-filled rocks following the observations made during the LAquila seismic sequence by⁶⁵.

As shown in the supplementary material (Fig. S6), during the four phases, it is possible to observe a predominant upward migration of seismicity from the base of the seismogenic layer, where the main events are also located.

CL-2 occurs about 3 months after the II phase of CL-1, while CL-3 is the last seismic episode associated with the CL group. The magnitude versus time and statistical indexes (Fig. 4e–f’’) show that they are classifiable as swarms. The migration velocity is about 0.6–0.9 km/d, and the diffusivity is ~1.5 m^2/s , evaluable only for CL-2 (Fig. 6). Differently from CL-1, CL-2 and CL-3 show one phase prevailing even if a further shorter phase is also identifiable in CL-2 pattern (Figs. 4, S5 and S6). The V_p/V_s ratios of CL-2 and CL-3 are similar and range from 1.88 to 1.89 (Fig. 7).

The main characteristics of the spatiotemporal evolution of SO-1-SO-3 are different from those described for CL-1-CL-3.

SO-1-SO-3 evolved during the time interval spanning from February to July 2013. On the 15th of February 2013, 30 foreshocks ($M_L^{\max} 2.1$) of the Sora main event ($M_W 5.0$, SO-1, 16 February) occurred near Sora town at a depth range of 18–21 km (Figs. S7a’). With a high-velocity migration (5 km/d), the seismic front progressively

upwards to ~17 km depth, where the mainshock enucleated (Fig. S6c). The evolution does not depict a diffusivity trend, and the Vp/Vs ratio reaches a very high value of ~2.

The day after, probably triggered by SO-1, SO-2 initiates to involve another volume, northeastward and shallower of SO-1. Like SO-1, the seismic front migrates upward with a velocity of 7 km/d at 12 km, showing an apparent high diffusivity behavior of 1.5 m²/s. The Vp/Vs ratio assumes the typical value of the central intra-Appennines areas⁴⁷.

SO-3 starts in March, contemporary with SO-2 for almost one month. It is the shallowest cluster in the study area (~5–6 km, Fig. S7), and the space-time evolution shows a slow diffusivity trend of 0.4 m²/s. The Vp/Vs ratio is the lowest observed in this study.

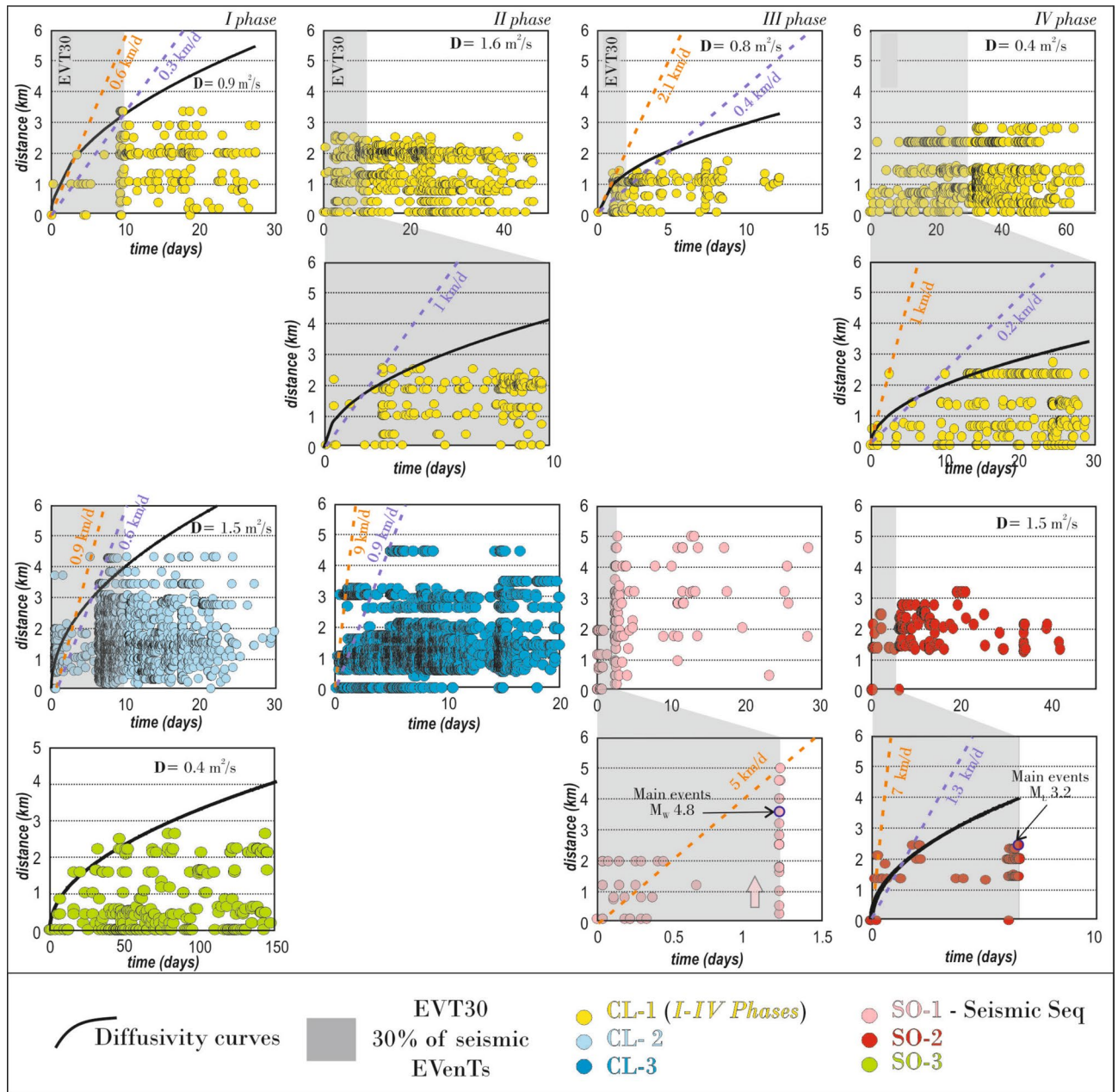


Figure 6. Time evolution of the 2010–2013 CL-1–CL-3, SO-1–SO-3. Time evolution versus the temporal distance of seismicity from the first event of the cluster considered as the reference point. The grey bands represent the first 30% of seismic events relative to the overall duration. The dotted lines indicate the constant rate or velocity migration expressed in km/d. The black curves represent the interpolation of the data selected as the 90th percentile in each considered bin within 30% of the overall duration of the single cluster, assuming the homogeneous 3D diffusion model of⁶⁴. The values of diffusivity along with their uncertainties are given in Table S2.

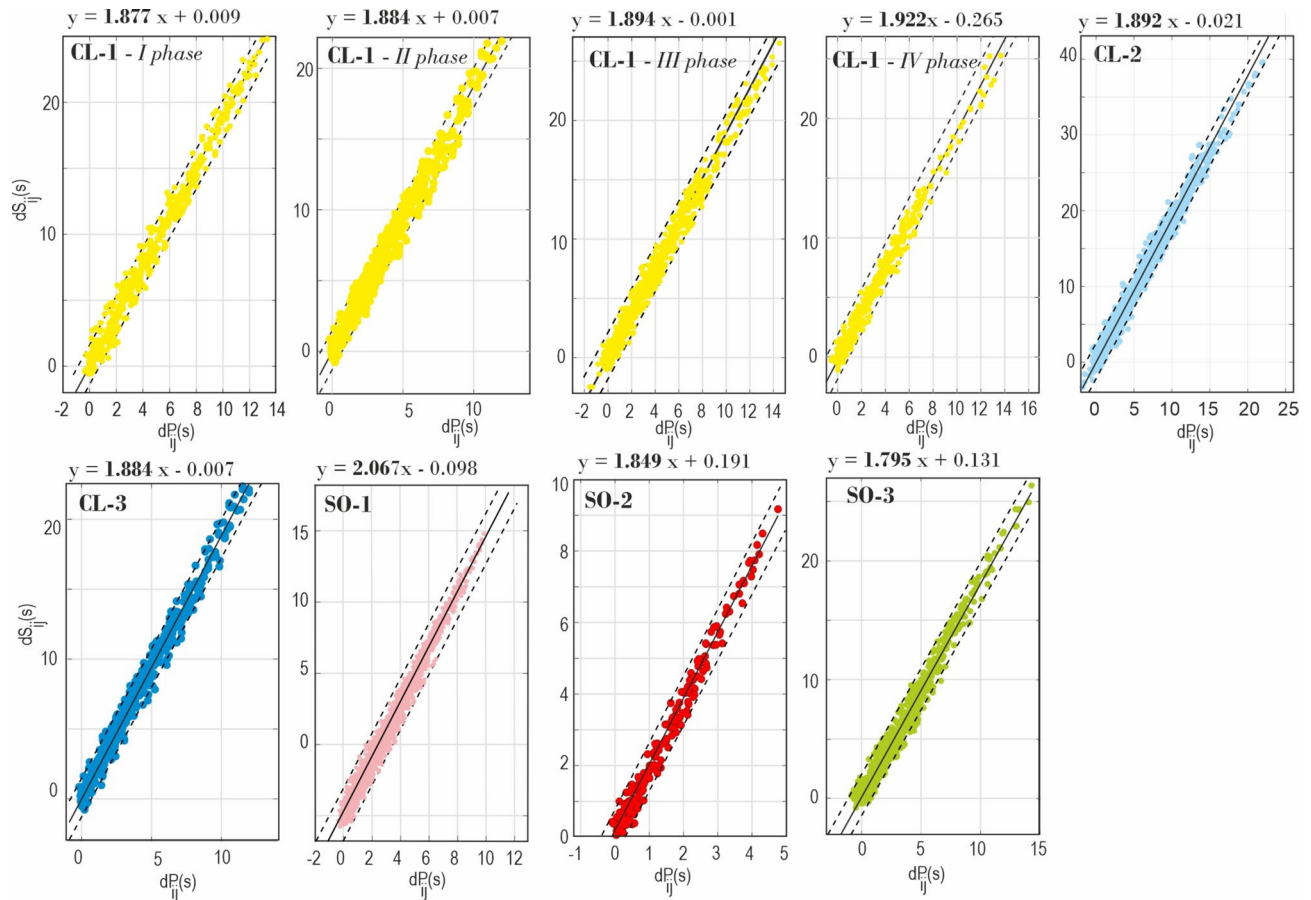


Figure 7. Modified Wadati diagram plots⁶⁶ computed using P- and S-arrival times of the Italian Seismic Bulletin⁵¹. Black dashed lines represent the standard deviation of the orthogonal regression. The values of V_p/V_s along with their uncertainties are given in Table S2.

3D fault models

The eight identified hypocentral clusters show differences not only in depth and seismological features but also in the shape of the hypocentral volume.

CL-1 is located approximately 60 km south of the main event of the L'Aquila seismic sequence, between the Villavallelonga and Balsorano active faults (Figs. 1 and 2). It comprises 2332 earthquakes occupying an elongated area, N-S striking, and ~ 4 km long. The 3D distribution of CL-1 well illuminates a high-angle, east-dipping volume, nonplanar surface. The seismicity migration depicts a surface that dips 63° toward the northeast (Fig. 8a) and seems to be associated with an antithetic fault of SW-dipping Villavallelonga's northern segment.

The seismic activity of phases I-IV is well confined within a depth range of ~ 11–13 km (80% of seismic events, Fig. S7a–d), and the main event of each phase is located at depths of ~ 12–13 km (Fig. S6a–c). The coeval background seismicity partially illuminates the high-angle Villavallelonga normal fault. These observations are significant as seismicity has not been recorded over the instrumental times.

The focal mechanisms of the major events ($M_L \sim 2.6$) (Fig. 4a–d) show strike-slip (left lateral) kinematics⁴⁸ with an average T axis trending NNE-SSW ($\sim N25^\circ$) slightly counterclockwise rotated to the NE-SW average T axes of the pseudo-focal mechanism derived from geological data^{24,25} and the regional stress field of central Italy³⁴. Cluster 1, with its four subclusters (phases I-IV), has a narrow and elongated sub-vertical shape.

CL-2-CL-5 are located ~ 10 km southeast of CL-1 between the Villavallelonga-Pescasseroli-San Donato V.C. and Posta Fibreno active faults (Figs. 2 and 3). On the map, CL-2 and CL-3 exhibit an elongated SW-NE shape, each spanning ~ 4 km. They have common extensional kinematics and are characterized by near planar hypocentral distribution (Fig. 8b). They are similar in shape and extent, all being small high-angle southwest-dipping extensional planar mesh (Fig. 9a–c). They are very close to each other (~ 2 km) and represent a set of SSW-dipping fault patches synthetic to the Pescasseroli-Villavallelonga southern segments. They deepened NNEward from a depth of 8 km, beneath CL-5, to a depth of 14 km, beneath CL-3. Specifically, a progressive deepening of seismicity is observed starting from CL-4 (8–10), CL-2 (9–12 km), CL-5 (12–13 km), CL-3 (12–15 km) (depth ranges represented in Fig. 9c, S6b and S7a'–b'). A low-angle N to NNE-dipping planar mesh interpolating the CL-2 to CL-5 bottom trace can be represented (Figs. 8b and 9c).

The focal mechanisms of the major events associated with CL-2 and CL-3 show normal kinematics, and as observed for CL-1, the average trend of T-axes (Fig. 9, Table S3) is ~ N35. There is a large dispersion of the T-axes

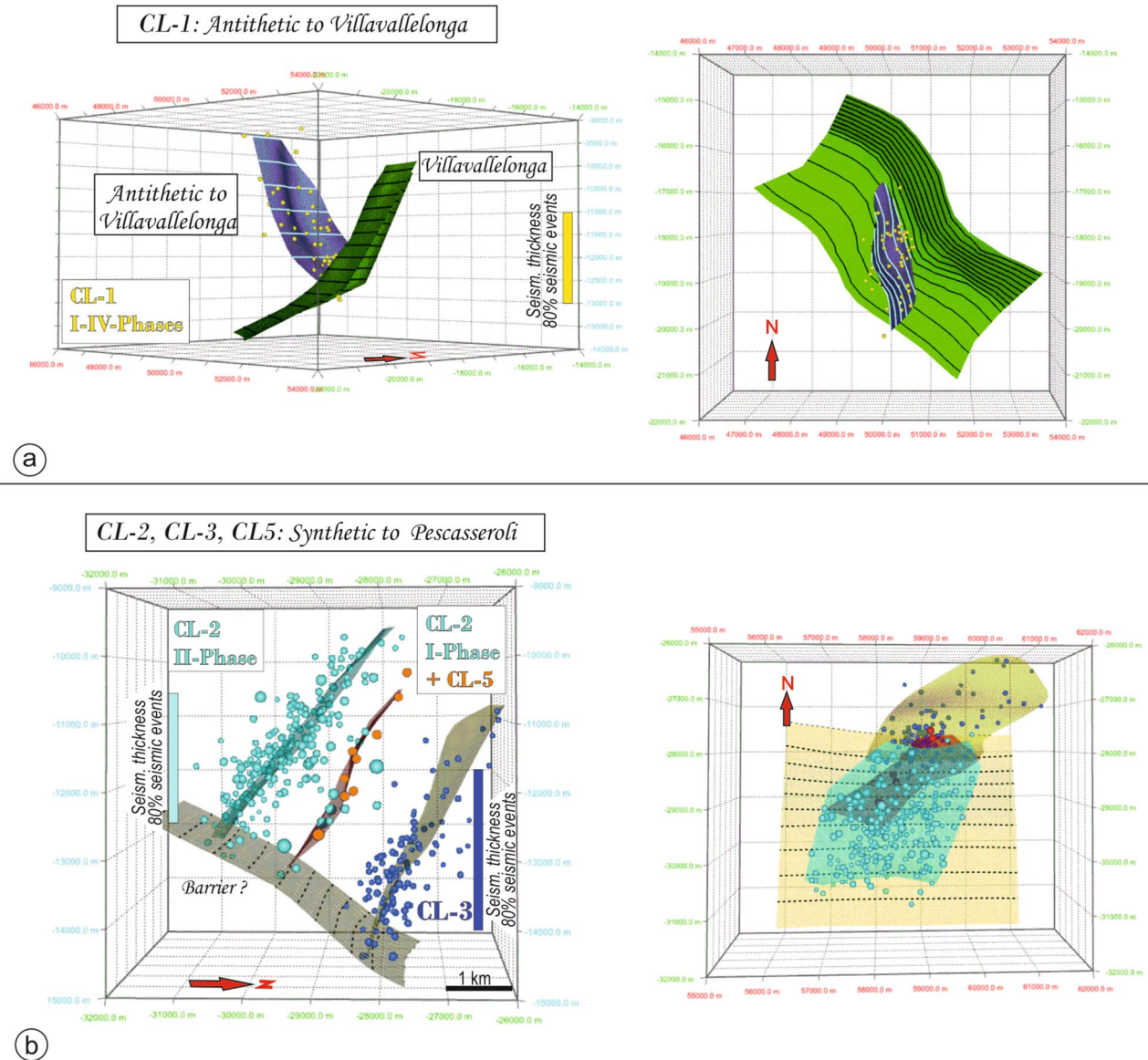


Figure 8. Section and map views of the reconstructed 3D models. Fault surfaces were built with the MOVE Suite software v. 2023 (Petroleum Experts Ltd) (a) 3D models and depth contour lines representing Villavallelonga and its antithetic faults, illuminated by CL-1, along with concurrent background seismicity (see Fig. 9d). (b) 3D models and depth contour lines depicting synthetic structures to the Villavallelonga-Pescasseroli alignment.

of focal mechanisms in Fig. 9 (white dots in the stereograms), probably due to the trend changing (from NW–SE to WNW–ESE) of the Villavallelonga-Pescasseroli faults (Figs. 2 and 9a).

SO-1–SO-3 are located around Sora, about 7 km south of CL-1 and 5 km west of CL-2 and CL-3 (Fig. 3). The 3D distribution of SO-1 and SO-2 does not evidence fault planes but vertical strips confined beneath the NNW-dipping basal detachment of the overlying CL-2 to CL-5 clusters. This configuration could suggest seismicity due to natural fluid injection (Fig. 9a–c).

Differently, SO-3 started in March and was contemporary with SO-2 for almost one month. It was the shallowest cluster in the study area (~5–7 km, Fig. S7). The 3D seismicity representation helps us to associate this episode with an antithetic structure of the Balsorano normal fault (section view in Fig. 9d).

The focal mechanisms⁴⁸ of the main seismic events of SO-1, SO-2, and SO-3 (Fig. 9e) show normal kinematics with average T-axes (N54, N51, N53, respectively) compatible with the regional stress field.

Discussion

From an earthquake process perspective, we investigate the spatiotemporal evolution of seismicity following the 2009 L'Aquila mainshock (M_w 6.3) in a high-seismic-risk area of southern-central Italy located about 60 km south of L'Aquila town. Thanks to the template-matching approach, we enhance the temporal resolution of

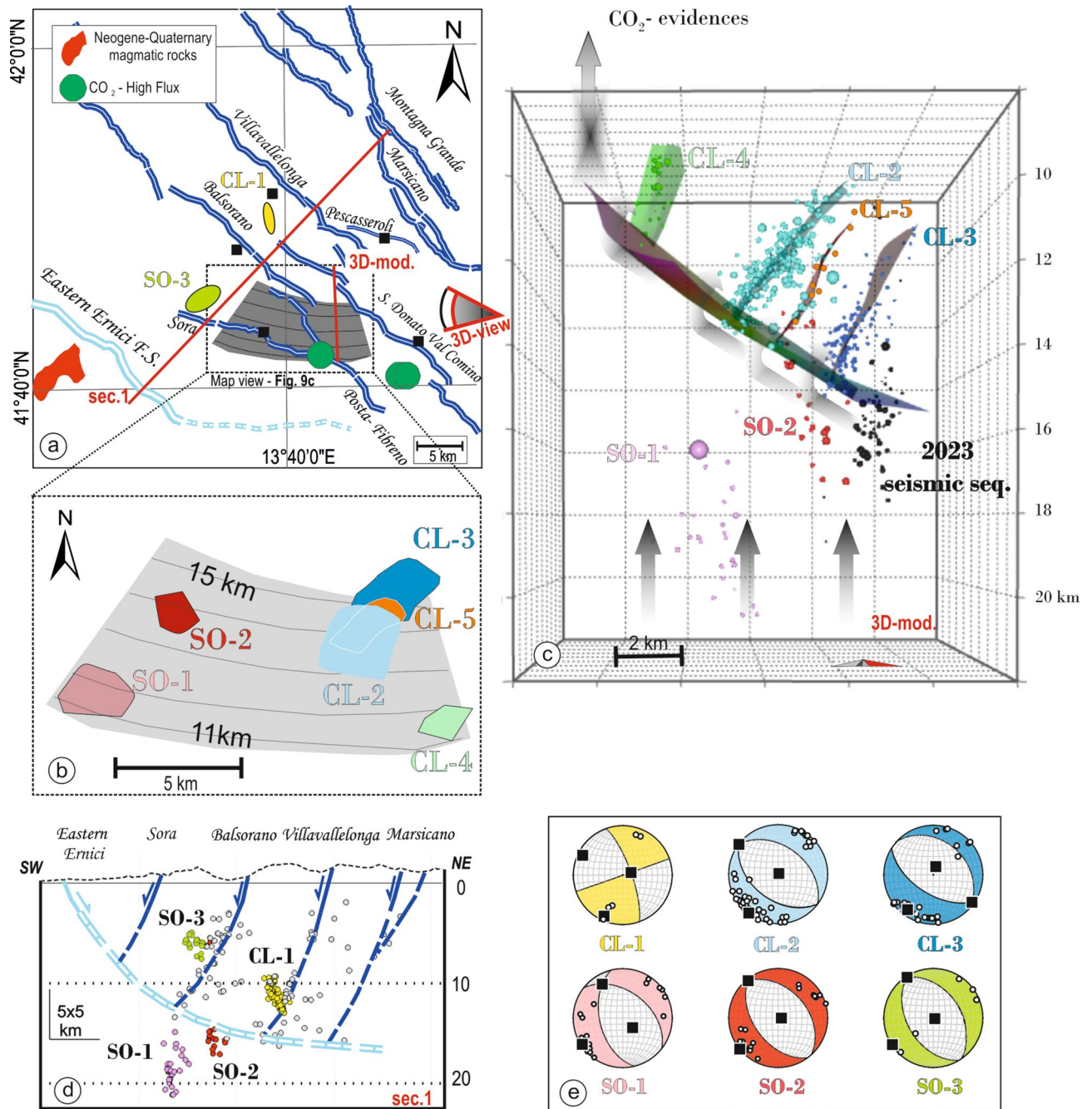


Figure 9. Picture of the main results (faults map is represented with ArcMap, by ESRI, ArcMap/ArcGIS, v. 10.8, <https://www.esri.com/en-us/home>, fault surfaces and cross-section with the MOVE Suite software v. 2023, Petroleum Experts Ltd). (a) Active fault systems, CO₂ measurements from⁵⁰, evidence of magmatic rocks, and CL-1 and SO-3. The grey area represents the WNW-ESE deformation band reconstructed using CL-2 to CL-5 clusters, and the red and grey symbol on the right represents the point of view of the 3D fault models. The red lines represent the traces of the section in panel (d) and the view of the 3D model (panel c). (b) Zoom of the WNW-ESE deformation band explicitly indicating the depth contour lines of the 3D reconstruction as in Fig. 9c and the distribution of analyzed clusters. (c) The 3D models showing the seismicity at the hanging wall and footwall of the basal detachment. (d) SW-NE section view of the seismicity from 2009 to 2013 with trace shown in Fig. 9a. (e) Average focal mechanisms (Table S2) related to CL-1-CL-3 and SO-1-SO-3, computed considering Frepoli et al.⁴⁸ data. Small circles plotted on the stereonets represent the T-axes of the single focal mechanisms, while black squares are the P, B, and T axes of the average ones.

seismicity, lowering the completeness magnitude by unmasking hidden earthquakes. The geometric-kinematics and clustering characteristics here investigated allow us 1) to gain insight into the physical processes that occurred

during the different stages of 2009–2013 seismic activity and 2) to contribute to better define the seismotectonic framework of an area characterized by extensional active faults. All the analyzed seismicity is highly controlled by fluid circulation at the upper and lower crust seismogenic layers, and multilayer extensional earthquakes characterize the study area.

Origin and Evolution of CL-1

The significant increment in seismic activity within the study region after the 2009 L'Aquila earthquake prompts an inquiry into the potential relation between the observed increase in seismicity and the mainshock of the L'Aquila seismic sequence.

Inferences of the L'Aquila earthquake on this sector of the Apennines were made by De Natale et al.⁶⁷. They highlighted the potentially anticipated reactivation of faults existing between the 1984 Barrea and the 2009 L'Aquila epicentral areas due to stress transfer from both earthquakes.

By analyzing the new catalog down to completeness magnitude ($M_c = 0$) and retrieving multiplets by template matching technique, we observe that CL-1 (I-Phase) occurs 34 h after the M_w 6.3 seismic event of L'Aquila, at ~60 km, raising the question of probable delayed dynamic triggering. The delayed dynamic triggering is debated in the literature because seismicity is continuously produced in seismic active regions. Generally, the remote triggering delay can be ascribed to several potential mechanisms, including surface waves that circumnavigate the Earth multiple times, waves that perturb and alter the frictional properties within a fault zone, or a process in which seismic waves open a fluid pressure valve, leading to the unlocking of a fault^{2,8,68,69}.

Moreover, Gomber and Johnson⁷⁰ observe that, similarly to laboratory experiments, remote triggering could result from large dynamic deformation like the ones produced by strong directivity.

On this matter, Calderoni et al.⁷¹ demonstrated that the earthquakes that occurred on the causative fault of the L'Aquila mainshock (i.e., Paganica fault in Fig. 1a) had strong unilateral directivity that largely affected the study area (Fig. S8a–b).

The seismic station nearest to CL-1 is Villavallelonga (VVLD), belonging to the National Seismic Network. The VVLD seismometer recorded a saturated seismic signal. In contrast, the nearest accelerometer, ORC, part of the Italian National Strong Motion Network⁷² (see Fig. S8a), located approximately 13 km northeast of CL-1, recorded a Peak Ground Velocity (PGV) exceeding the threshold identified by⁷⁰ Fig. S8c. These authors suggest that areas undergoing large PGVs exceeding the values of the experimental curve, representing the scaling of dynamic deformations with the distance, could be susceptible to dynamic triggering.

These considerations, combined with the observation that the enhanced catalog ensures the absence of smaller or larger events responsible for primary triggering in the study area, make the delayed dynamic triggering effect a good candidate for explaining the genesis of CL-1. Specifically, the early CL-1 phase, comprising some hundred seismic events, intermittently promoted the other CL-phases, characterized by ~2000 earthquakes. This fluid circulation could promote the occurrence of other clusters (CL-2, CL-3) of seismicity (section “[The role of fluid in triggering CL-2-CL-3 and SO-1-SO-2](#)”).

The role of fluid in triggering CL-2-CL-3 and SO-1-SO-2

Recent seismological, geochemical, and hydrogeochemical literature illustrates how fluid circulation, originating from various sources within the crust or mantle in the Apennines, can potentially promote seismic events and exert influence over the entire seismic cycle^{41,73–78}.

Our observations show that extensional earthquakes can occur at different seismogenic layers (Fig. 9), and the results support the hypothesis that fluids play an essential role in the processes controlling the cascade of the observed seismic episodes.

The presence of fluids is fully confirmed by direct measures of CO₂ flux⁵⁰. Three degassing sites classified as “very high flux” were found just in the proximity of the CL-2-CL-3 epicentral areas (green circles in Fig. 9a). Ciotoli et al.⁷⁹ measure an ongoing degassing of deep endogenic gases (Helium and Radon anomalies) along the Val Roveto Valley, North of Balsorano–Posta Fibreno fault system. Moreover, Smeraglia et al.⁴¹ find insights into fluid circulation at the upper and lower crust by analyzing calcite-filled comb and slip parallel fractured veins on the Balsorano-Posta Fibreno faults alignment.

The high diffusivity values, resulting from our analysis, indicate that fluids could circulate through more fractured or permeable rocks at depths. In such conditions, seismogenic fault systems can represent a preferential pathway for fluid mobility⁸⁰.

Based on these considerations, we suggest that the mainshock of the L'Aquila seismic sequence could have modified the frictional properties in the Villavallelonga fault zones (Fig. 8) or opened a fluid pressure valve^{2,7,68,69} sealed by mineral depositions or other chemical processes. High-pressure fluids could favor the occurrence of the CL-1 phases and the other intermittent phases until 2012 (Fig. S5) following the overpressure pulses migration upward along the fault as modeled by¹¹. The fluid circulation, controlled by the major seismogenic faults, has promoted the delayed seismic activity of CL-2, CL-3, and other minor clusters in the crystalline basement.

The 3D position relative to the active fault alignments of Villavallelonga-San Donato Val Comino and Balsorano-Posta Fibreno and the depth range occupied by the hypocenters in the lower crust suggest that the genesis of SO-1 to SO-2 is different and independent from CL-1-CL-3. The spatial reconstruction of SO-1 bears similarity with the 3D geometry of the seismic sequence that occurred in 2013–2014, ~60 km southeast of SO-1 in the southern Matese region (M_w^{\max} 5.2) (Figs. 1a and S1a). This area, characterized by high attenuation values^{36,81}, provides evidence that the triggering mechanisms of these earthquakes are associated with magmatic intrusion. Our findings concerning the spatiotemporal evolution, the high migration velocity, the V_p/V_s ratio, and the depth geometry indicate that SO-1 might be controlled by ascending mantle fluids possibly originating from degassing magmatic intrusions as observed in the study area^{41,50,79}. Hints of volcanic processes (e.g., sparse magmatic

outcrops) are present in proximity to the volcanic districts of the Ernici Mountains (Fig. 9a). The spectrograms of the main event (Fig. S9) show some signs but no clear evidence of the low-frequency content typical of similar earthquakes. However, we lack additional information to distinguish the triggering mechanisms definitively. In this scenario, we suggest that SO-2 and SO-3 can have been triggered in turn by SO-1.

3D tectonic control in seismic sequence evolution

Multiphase swarms and complex seismic sequences characterize the analyzed seismicity. This seismic activity involves multiple segments in a cascading mechanism, including synthetic and antithetic faults to major structures (Fig. 9a–e), and clusters (SO-1, SO-2) that are not directly correlated with tectonic structures and that show geometric warping along strike and dip.

Such a complex pattern, with interconnected multi-scale synthetic and antithetic faults, involves small-magnitude seismic events ($M_L < 4.8$) but exhibits similarities with both the outcropping extensional structures of the Apennine fault systems and the spatiotemporal evolution of recent large earthquakes: Irpinia 1980, Colfiorito 1997, L'Aquila 2009, and Amatrice, Visso, and Norcia 2016–2017. These major events involve the failure of multiple critically stressed faults or fault segments, which, in turn, influence the duration and evolution of seismic activity.

Our results allow us to distinguish three cluster typologies concerning active faults:

Type 1—clusters on secondary structures antithetic to major faults, generally located close to the intersection with the main faults (i.e., CL-1, SO-3);

Type 2—clusters on major faults in specific positions, for example, close to the basal detachment or at synthetic fault intersections (i.e., CL-2–CL5);

Type 3—clusters not directly controlled by tectonics (i.e., SO-1, SO-2).

Type 1. CL-1 and SO-3 illuminated fault segments antithetical to the Villavallelonga and Balsorano faults, respectively (Fig. 9d). The two major faults were partially imaged through a synchronous mechanism of background seismicity. These observations further corroborate the pivotal role of antithetic faults in accommodating deformation and promoting interactions between antithetic and principal fault systems during seismic sequences, as observed in the 2016–2017 Central Italy seismic sequence^{57,82}, in the foreshock sequence of the 2009 L'Aquila earthquake^{83–86} and during the Balsorano minor seismic sequence of 2019 ($M_W^{\max} 4.6$)⁸⁷.

It is conceivable that the discontinuity associated with CL-1 resembles the Annifo segment of the Colfiorito sequence³⁴. In that instance, the seismogenic N-S left-lateral fault inverted a pre-existing right-lateral structure formed during the Late Miocene–Pliocene compressional phase. Similarly, CL-1-related discontinuity could be originally a pre-existing right-lateral fault, subsequently reactivated with left-lateral shear within an extensional stress field. The affected volume, seemingly detaching along the southwest-dipping Villavallelonga fault, undergoes deformation characterized by a pure strike-slip regime with a nearly NNE–SSW oriented T-axis (see Fig. 9e). This strike-slip kinematics occur within the context of a purely regional extensional pattern.

Type 2. CL-2, CL-3, CL-4, and CL-5 nucleated on the lower portion of major WSW- to SSW-dipping Quaternary faults, extending upward for some kilometers from the intersection with the common basal detachment (Fig. 9c). The envelope of the base of the seismogenic layer of CL-2–CL-5 may be well interpolated by a planar surface dipping N-ward to NNE-ward with a dip angle of about 35° at depths from ~12 to ~15 km (Fig. 8). The spatial position of the reconstructed SSW-dipping parallel seismogenic patches (Fig. 9c) that are high-confined, and spaced a few kilometers perpendicular to the strike, suggest a leading role played by such N-dipping discontinuity. Following the reasoning of⁸⁸, we advance the hypothesis that such basal surface could have played essential role in driving seismicity. By undulating along-dip channels (e.g., tectonic mega groves), the natural fluid could be injected at the base of the fault zone, thus activating small portions of parallel antithetic structures.

A peculiarity of the 3D seismogenic fault mesh corresponding to these clusters (Fig. 9) is the length/width shape ratio, which is always <1 due to a greater extent along the dip than along the length. This configuration supports the hypothesis that fluids naturally injected into the fault zone from below are diffused through dip-parallel channels while triggering earthquakes. This basal detachment surface can play the role of a transitory barrier or may be interpreted as a relevant tectonic structure connected with the Ernici NE to N-dipping extensional fault system (Fig. 9). In such a case, all the major SW- to SSW-dipping Quaternary normal faults of the study area would represent first-order antithetic splays to such a basement discontinuity. A similar geometric configuration is already highlighted from active and passive seismic data for the Eastern Sabini extensional fault system at the bottom of the Paganica fault system, responsible for the L'Aquila earthquake³⁰, besides the well-known Altotiberina low-angle normal fault⁸⁹.

Type 3. SO-1 and SO-2, as well as a very recent sequence that occurred in the same area in November 2023 ($M_L^{\max} 2.8$, depth 16 km), not considered in this study, are confined within the crystalline basement in the lower crust at the footwall of the NNE-dipping reconstructed discontinuity (Fig. 9c). These clusters do not appear to be controlled by a well-specific tectonic structure but rather by a mixture of sub-vertical channeling and pressure changes due to the ascent of mantle fluids or even melt. The spatiotemporal behavior and 3D reconstruction identify two in-space and time-close episodes of near-vertical strips of earthquakes rising from about 20 km up to 10 km (SO-1, SO-2). The overall 3D reconstruction (Fig. 9) allowed us to identify a deep seismogenic layer capable of generating earthquakes of significant magnitude for the area. These earthquakes are expressions of the regional extensional stress field and can produce additional seismicity in the Apennine area, independent from the main upper crust extensional system, increasing the seismic hazard of the study area.

Conclusions

The comprehensive analysis of dynamic seismic processes observed from 2009 to 2013, combined with geological data, enables us to characterize the typology of seismicity in a high seismic hazard area during an inter-seismic period and to reveal a previously unrecognized deformation zone. This zone spans 15 km in a WNW-ESE direction, that is lined up with the characteristic trends of the Pescasseroli and Sora faults (Fig. 9). Within this region, seismicity patterns depict a network of synthetic faults gradually converging along a 35° north-dipping plane, potentially serving as a permeability barrier or a low-angle normal fault associated with the Ernici fault systems.

Our analyses suggest that the north-dipping plane may be crucial in guiding mantle fluids in this region. These fluids enhance the seismic process, a conclusion backed by direct surface measurements from various studies^{41,50}.

The reconstructed configuration indicates the existence of two overlapping extensional seismogenic domains. The first seismogenic layer extends from the outcropping faults to the crystalline basement, while the second layer stands in the lower crust. Consequently, earthquakes originating in this area can be correlated with the complex outcropping pattern of active faults and deeper earthquakes, such as the Sora seismic sequence. The second deeper seismogenic layer, capable of releasing moderate earthquakes (at least from what has been observed so far through historical and instrumental earthquakes), exacerbates the seismic scenarios in this high seismic hazard sector of the central Apennine.

We are confident that our findings offer valuable insights, marking a significant advancement in the field. They serve as a pivotal reference, steering upcoming research toward developing advanced seismotectonic models. These enhanced models will seamlessly incorporate tectonic data and seismic activity, comprehensively characterizing seismic processes.

Methods

Template matching

To enhance the seismic catalog of the earthquakes that occurred in the study area after the 2009 L'Aquila earthquake, we selected as templates the 856 relocated events of the Catalog of Absolute (nonlinear) 3D earthquake Locations (CLASS)^{17,51} with horizontal errors < 3 km and vertical errors < 4 km (Fig. 3). Average horizontal and vertical errors are 0.5 and 1.5 km, respectively. RMS errors of the travel time residuals are less than 0.4 s and templates have an azimuthal gap less than 270°.

We use the open-source seismological package PyMPA^{77,90}, which detects microseismicity from cross-correlation of continuous data and templates. PyMPA was used in previous applications, such as for processing recent seismic sequences in Italy^{84,91}.

Template matching is applied to 4 years of continuous data recorded at 7 permanent three-component seismic stations (VVLD, INTR, LPEL, CERA, GUAR, POFI, PTQR) of the Italian National Seismic Network (Fig. S3) for searching hidden earthquakes that resemble well-located events. Continuous data are downsampled to 50 Hz and trimmed to 5 s starting 2.5 s before the theoretical S wave arrival, calculated using the velocity model derived from⁴⁷. The waveforms are also filtered from 3 to 15 Hz to enhance the signal-to-noise ratio of local earthquakes.

Templates are also evaluated by adopting Kurtosis-based tests⁹² to select an optimal signal-to-noise ratio, avoiding using blurred signals in the matching technique. Earthquake magnitudes for the enhanced catalog are calculated relative to the magnitude of master events, given in the original CLASS catalog, considering that the scalar moments of two events with similar waveforms scale as the amplitudes of their waveforms.

The location of the small events in the augmented catalog strictly depends on the quality of the input catalog locations and associated errors. Due to the high resolution of the starting catalog, we decided to keep the new detections co-located with the templates.

This choice of not relocating the new events is partly justified by the area dimensions, the seismic station inter-distance relative to the area under study, and the reduced number of earthquakes for which it is possible to obtain a more refined location.⁹³ and ⁹⁴ demonstrated that only a small portion of events from template matching could be relocated (on average less than 20%). Moreover, relocation techniques based on limited frequency-band envelopes⁹¹ cannot improve the location of small-magnitude events when the network coverage is sparse. These considerations led us to collocate the new events at the respective template positions.

Data Analysis

Declustering

The first step in the cluster analysis is to apply the Zaliapin declustering method for separating background from clustered seismicity⁶⁰.

The nearest-neighbor method computes the time-space distance between pairs of earthquakes. Rescaled time (T) and distance (R) between an event and its parent are normalized by the magnitude of the parent. The empirical distributions of the logarithm of the nearest-neighbor distance, $\log_{10} \eta^*$, and their components (T, R) are shown in Fig. 3d. It is worth noting that the co-location of new detections with their templates results in R_{ij} becoming zero, leaving $\log(T_{ij})$ as the sole component for calculating the bidimensional spatiotemporal distance in the Zaliapin and Ben-Zion framework. This aspect leads to a trimodal pattern in the (T, R) plane that does not affect the declustering process. Combining the nearest neighbor method with the analysis of interevent times is effective for segregating events that are independent even if co-located, as shown in⁶¹.

After this, we can classify the most important clusters in swarms or seismic sequences as a function of their signature features.

In addition, we use the Gardner windowing method⁹⁵ to separate different temporal phases.

Using the distribution of interevent times for spatially close events, we check if some multi-modality can suggest how to separate the related events from the independent ones. Results from this analysis, performed for some clusters, evidence that the problem does not affect our results. However, we notice that some events can

be included in the same cluster, even if the cluster activity is off for some time and reactivates later. To overcome this problem, we rank clusters into sub-clusters or phases at similar positions using⁹⁵ windowing.

Subsequently, all clusters and temporal phases within are classified into swarms, mainshock-aftershock, and foreshock-mainshock sequences following the criterion proposed by⁶². The mainshock is the strongest earthquake in a cluster, and all the previous seismic events are pre-shocks. All pre-shocks are set foreshocks when the magnitude gap between the largest pre-shock and the mainshock is greater than 0.5. Unlike, a swarm-like sequence has pre-shocks with similar magnitudes (the difference is smaller than 0.5).

Statistical indexes

To characterize the clustered seismicity, (1) we plot the magnitude versus time and classify the cluster as a swarm (S), foreshocks-mainshock-aftershocks (FMA), or mainshock-aftershocks (MA) considering the⁶² approach, we evaluate (2) the temporal evolution of the coefficient of variation of interevent times, and (3) the seismic moment ratio.

Coefficient of variation of interevent times

Studying the interevent times (τ) and their covariance (Cv) is very useful to quantify temporal clustering or the degree of periodicity in earthquake occurrence. Cv is the standard deviation of interevent times (σ) and the mean interevent time (μ) ratio. Periodic and quasi-periodic events have values of $0 < Cv < 1$, random Poisson processes have $Cv \sim 1$, and temporally clustered earthquakes $Cv > 1$ ⁹⁶⁻⁹⁸.

We compute Cv for each cluster using a sliding window. We repeat this computation considering six windows with lengths varying from 5 to 15% of the total events with an incremental step of 2%. For each window, we calculate the mean and standard deviation (σ) of the interevent time (τ) to determine the coefficient of variation. The final step is estimating the mean value and standard deviation of the coefficient of variation resulting from the six different windows.

Seismic moment ratio temporal evolution

The Seismic Moment Ratio evolution (SMR) over time⁹⁹ defines the presence of main phases of seismicity in terms of the maximum release of energy. This index over time is significantly different for regular seismic sequences and swarms. SMR varies from 0 to 1, and values close to ~ 1 mean that the clustered seismicity has a seismic sequence behavior with a single dominating event.

As for the Cv , we evaluate SMR for each cluster using a sliding window, and we repeat this operation considering six different windows.

We preliminarily convert the magnitude of the events from M_L to M_w by using the relation proposed by¹⁰⁰ for small earthquakes ($M_w = \frac{2}{3}M_L + C'$) and compute the seismic moment considering¹⁰¹ relationship ($M_w = \frac{2}{3} \log_{10}(M_0) - 6.07$).

Then, we calculate, for each window, the highest value of the seismic moment, the sum of the seismic moment of the events, and the ratio between these two parameters.

The final step is calculating the mean value and standard deviation of the ratio between the maximum seismic moment and the sum of the seismic moments of the events for the six, different windowing to obtain one single curve over time.

Migration velocities of the Seismicity and V_p/V_s ratio

The reconstruction of the migration velocities of the seismicity in space-time is particularly complex. It allows us to observe the presence of seismic fronts and calculate the average migration velocity to keep the mechanism of the genesis of seismic swarms.

We can determine in the seismic cluster and swarm activity a preferential direction of growth of the seismicity with different activity rates during the time. Following¹⁰², to compute the migration velocity and precisely the early stage of hypocenter migration, we:

- (1) Calculate the distance of the seismic events to the first seismic event;
- (2) Select the distance data as the 90th percentile in each considered bin falling within 30% of the overall duration of the single episode;
- (3) Compute the straight line's angular coefficient connecting the first and the farthest event.

Moreover, we consider the events selected at point 2) and interpolate them by fitting the diffusion model proposed by⁶⁴ over a regular grid of values.

3D model building

To build the 3D fault models, we consider the cluster hypocentral distribution and, where possible, apply the following multistep analysis.

(1-2) We select the earthquakes falling within the depth layer encompassing approximately 80% of seismic events, and we define an initial mesh by interpolating the selected hypocenters via the Inverse Distance Weight (IDW) method, employing a power inverse distance exponent value set at 0.5.

(3) We draw contour lines based on the initial mesh representing depth increments of 500 m.

(4) Then, we resample the depth contour lines at a consistent 500 m interval to achieve smoother lines.

We generate the final curvilinear mesh using either Delaunay Triangulation or Spline curves and apply them to the resampled contour lines.

Data availability

Data is provided within the supplementary information files.

Received: 13 February 2024; Accepted: 31 July 2024

Published online: 07 August 2024

References

1. Freed, A. M. Earthquake triggering by static, dynamic, and postseismic stress transfer. *Annu. Rev. Earth Planet. Sci.* **33**, 335–367 (2005).
2. Gomberg, J., Blanpied, M. L. & Beeler, N. M. Transient triggering of near and distant earthquakes. *Bull. Seismol. Soc. Am.* **87**, 294–309 (1997).
3. Harris, R. A. Introduction to special section: Stress triggers, stress shadows, and implications for seismic hazard. *J. Geophys. Res. Solid Earth* **103**, 24347–24358 (1998).
4. Brodsky, E. E. & Van Der Elst, N. J. The uses of dynamic earthquake triggering. *Annu. Rev. Earth Planet. Sci.* **42**, 317–339 (2014).
5. Fan, W., Barbour, A. J., Cochran, E. S. & Lin, G. Characteristics of frequent dynamic triggering of microearthquakes in Southern California. *J. Geophys. Res. Solid Earth* **126**, e2020JB020820 (2021).
6. Bodin, P. & Gomberg, J. Triggered seismicity and deformation between the Landers, California, and Little Skull Mountain, Nevada, earthquakes. *Bull. Seismol. Soc. Am.* **84**, 835–843 (1994).
7. Sibson, R. H. Conditions for fault-valve behaviour. *Geol. Soc. Lond. Spec. Publ.* **54**, 15–28 (1990).
8. Brodsky, E. E., Roeloffs, E., Woodcock, D., Gall, I. & Manga, M. A mechanism for sustained groundwater pressure changes induced by distant earthquakes. *J. Geophys. Res. Solid Earth* **108**, 2002JB002321 (2003).
9. Parsons, T. A hypothesis for delayed dynamic earthquake triggering. *Geophys. Res. Lett.* **32**, 2004GL021811 (2005).
10. Parsons, T., Malagnini, L. & Akinci, A. Nucleation speed limit on remote fluid-induced earthquakes. *Sci. Adv.* **3**, e1700660 (2017).
11. Zhu, W., Allison, K. L., Dunham, E. M. & Yang, Y. Fault valving and pore pressure evolution in simulations of earthquake sequences and aseismic slip. *Nat. Commun.* **11**, 4833 (2020).
12. Belardinelli, M. E., Bizzarri, A. & Cocco, M. Earthquake triggering by static and dynamic stress changes. *J. Geophys. Res. Solid Earth* **108**, 2002JB001779 (2003).
13. Llenos, A. L., McGuire, J. J. & Ogata, Y. Modeling seismic swarms triggered by aseismic transients. *Earth Planet. Sci. Lett.* **281**, 59–69 (2009).
14. Kato, A. *et al.* Propagation of slow slip leading up to the 2011 M 9.0 Tohoku–Oki earthquake. *Science* **335**, 705–708 (2012).
15. Schurr, B. *et al.* Gradual unlocking of plate boundary controlled initiation of the 2014 Iquique earthquake. *Nature* **512**, 299–302 (2014).
16. Pondrelli, S., Salimbeni, S., Perfetti, P. & Danecek, P. Quick regional centroid moment tensor solutions for the Emilia 2012 (northern Italy) seismic sequence. *Ann. Geophys.* **55**, 13 (2012).
17. Latorre, D., Di Stefano, R., Castello, B., Michele, M. & Chiaraluce, L. An updated view of the Italian seismicity from probabilistic location in 3D velocity models: The 1981–2018 Italian catalog of absolute earthquake locations (CLASS). *Tectonophysics* **846**, 229664 (2023).
18. Lavecchia, G. *et al.* Regional seismotectonic zonation of hydrocarbon fields in active thrust belts: A case study from Italy. In *Building knowledge for Geohazard assessment and management in the caucasus and other orogenic regions* (eds Bonali, F. L. *et al.*) 89–128 (Springer, Netherlands, 2021).
19. Mariucci, M. T. & Montone, P. Database of Italian present-day stress indicators, IPSI 1.4. *Sci. Data* **7**, 298 (2020).
20. Mariucci, M. T. & Montone, P. IPSI 1.5, Italian present-day stress indicators dataset. (2022) <https://doi.org/10.13127/IPSI.1.5>.
21. ISDe Working Group. Italian seismological instrumental and parametric database (ISDe). (2007) <https://doi.org/10.13127/ISIDE>
22. Rovida, A., Locati, M., Camassi, R., Lolli, B. & Gasperini, P. The Italian earthquake catalogue CPTI15. *Bull. Earthq. Eng.* **18**, 2953–2984 (2020).
23. Rovida, A. *et al.* Catalogo Parametrico dei Terremoti Italiani (CPTI15), versione 4.0. 4894 earthquakes Istituto Nazionale di Geofisica e Vulcanologia (INGV) <https://doi.org/10.13127/CPTI/CPTI15.4> (2022).
24. Lavecchia, G. *et al.* QUIN 2.0 - new release of the data descriptor Quaternary fault strain Indicators database from the Southern Apennines of Italy. *Sci. Data* **11**(1), 189 (2024).
25. Lavecchia, G. *et al.* Quaternary fault strain Indicators database - QUIN 1.0 - first release from the Apennines of central Italy. *Sci. Data* **9**, 204 (2022).
26. Maceroni, D. *et al.* First evidence of the late pleistocene—holocene activity of the Roveto Valley Fault (Central Apennines, Italy). *Front. Earth Sci.* **10**, 1018737 (2022).
27. Devoti, R. *et al.* A combined velocity field of the mediterranean region. *Ann. Geophys.* **60**, 1 (2017).
28. Serpelloni, E. *et al.* Surface velocities and strain-rates in the euro-mediterranean region from massive GPS data processing. *Front. Earth Sci.* **10**, 907897 (2022).
29. Mirabella, F., Brozzetti, F., Lupattelli, A. & Barchi, M. R. Tectonic evolution of a low-angle extensional fault system from restored cross-sections in the Northern Apennines (Italy). *Tectonics* **30**, 2011TC002890 (2011).
30. Lavecchia, G. *et al.* Multidisciplinary inferences on a newly recognized active east-dipping extensional system in Central Italy. *Terra Nova* **29**, 77–89 (2017).
31. Cirillo, D. *et al.* Structural complexities and tectonic barriers controlling recent seismic activity in the Pollino area (Calabria–Lucania, southern Italy) – constraints from stress inversion and 3D fault model building. *Solid Earth* **13**, 205–228 (2022).
32. Brozzetti, F. *et al.* Structural style of Quaternary extension in the Crati Valley (Calabrian Arc): Evidence in support of an east-dipping detachment fault. *Ital. J. Geosci.* **136**, 434–453 (2017).
33. D’Amico, S. *et al.* Seismic moment tensors and regional stress in the area of the December 2013–January 2014, Matese earthquake sequence (Italy). *J. Geodyn.* **82**, 118–124 (2014).
34. Ferrarini, F., Lavecchia, G., De Nardis, R. & Brozzetti, F. Fault geometry and active stress from earthquakes and field geology data analysis: The Colfiorito 1997 and L’Aquila 2009 cases (Central Italy). *Pure Appl. Geophys.* **172**, 1079–1103 (2015).
35. Trionfera, B., Frepoli, A., De Luca, G., De Gori, P. & Dogliani, C. The 2013–2018 matese and beneventano seismic sequences (Central–Southern Apennines): New constraints on the hypocentral depth determination. *Geosciences* **10**, 17 (2019).
36. Di Luccio, F. *et al.* Seismic signature of active intrusions in mountain chains. *Sci. Adv.* **4**, e1701825 (2018).
37. Lavecchia, G. *et al.* The April 2009 L’Aquila (central Italy) seismic sequence (Mw 6.3): A preliminary seismotectonic picture. *Recent Prog. Earthq. Geol.* 1–17 (2011).
38. DISS Working Group. Database of Individual Seismogenic Sources (DISS), version 3.3.0: A compilation of potential sources for earthquakes larger than M 5.5 in Italy and surrounding areas. 132 Individual Seismogenic Sources, 197 Composite Seismogenic Sources, 38 Debated Seismogenic Sources, 4 Subduction Zones (2021) <https://doi.org/10.13127/DISS3.3.0>.
39. Galadini, F. & Messina, P. Early–Middle Pleistocene eastward migration of the Abruzzi Apennine (central Italy) extensional domain. *J. Geodyn.* **37**, 57–81 (2004).

40. Papanikolaou, I. D., Roberts, G. P. & Michetti, A. M. Fault scarps and deformation rates in Lazio-Abruzzo, Central Italy: Comparison between geological fault slip-rate and GPS data. *Tectonophysics* **408**, 147–176 (2005).
41. Smeraglia, L. *et al.* Crustal-scale fluid circulation and co-seismic shallow comb-veining along the longest normal fault of the central Apennines. *Italy. Earth Planet. Sci. Lett.* **498**, 152–168 (2018).
42. Carafa, M. M. C. *et al.* Partitioning the ongoing extension of the Central Apennines (Italy): Fault slip rates and bulk deformation rates from geodetic and stress data. *J. Geophys. Res. Solid Earth* **125**, e2019JB018956 (2020).
43. ITHACA Working Group. ITHACA (ITaly HAZard from CApable faulting), A database of active capable faults of the Italian territory. (2019).
44. Cucci, L. & Cinti, F. R. In search of the 1654 seismic source (Central Italy): An obscure, strong, damaging earthquake occurred less than 100 km from Rome and Naples. *Appl. Sci.* **12**, 1150 (2022).
45. D'Agostino, N. *et al.* Contemporary crustal extension in the Umbria–Marche Apennines from regional CGPS networks and comparison between geodetic and seismic deformation. *Tectonophysics* **476**, 3–12 (2009).
46. Bagh, S. *et al.* Background seismicity in the Central Apennines of Italy: The Abruzzo region case study. *Tectonophysics* **444**, 80–92 (2007).
47. Romano, M. A. *et al.* Temporary seismic monitoring of the Sulmona area (Abruzzo, Italy): A quality study of microearthquake locations. *Nat. Hazards Earth Syst. Sci.* **13**, 2727–2744 (2013).
48. Frepoli, A. *et al.* Seismic sequences and swarms in the Latium–Abruzzo–Molise Apennines (central Italy): New observations and analysis from a dense monitoring of the recent activity. *Tectonophysics* **712–713**, 312–329 (2017).
49. Vedova, B. D., Bellani, S., Pellis, G. & Squarci, P. Deep temperatures and surface heat flow distribution. In *Anatomy of an Orogen the Apennines and Adjacent Mediterranean Basins* (eds Vai, G. B. & Martini, I. P.) 65–76 (Springer, 2001).
50. Frondini, F. *et al.* Measuring and interpreting CO₂ fluxes at regional scale: the case of the Apennines. *Italy. J. Geol. Soc.* **176**, 408–416 (2019).
51. Latorre, D., Di Stefano, R., Castello, B., Michele, M. & Chiaraluze, L. Catalogo delle Localizzazioni ASSolute (CLASS). 64 MB Istituto Nazionale di Geofisica e Vulcanologia (INGV) <https://doi.org/10.13127/CLASS.1.0> (2022).
52. Matthews, D. L., Rosenberg, T. J., Benbrook, J. R. & Bering, E. A. Dayside energetic electron precipitation over the South Pole ($\lambda = 75^\circ$). *J. Geophys. Res. Space Phys.* **93**, 12941–12945 (1988).
53. Amato, A. & Mele, F. M. Performance of the INGV national seismic network from 1997 to 2007. *Perform. INGV Natl. Seism. Netw. 1997 2007 Annals of Geophysics*, 15 (2008).
54. Boncio, P., Brozzetti, F. & Lavecchia, G. Architecture and seismotectonics of a regional low-angle normal fault zone in central Italy. *Tectonics* **19**, 1038–1055 (2000).
55. Collettini, C. & Barchi, M. R. A low-angle normal fault in the Umbria region (Central Italy): A mechanical model for the related microseismicity. *Tectonophysics* **359**, 97–115 (2002).
56. Brozzetti, F. The Campania–Lucania extensional fault system, southern Italy: A suggestion for a uniform model of active extension in the Italian Apennines. *Tectonics* **30**, 2010TC002794 (2011).
57. Improta, L. *et al.* Multi-segment rupture of the 2016 Amatrice–Visso–Norcia seismic sequence (central Italy) constrained by the first high-quality catalog of early aftershocks. *Sci. Rep.* **9**, 6921 (2019).
58. Bello, S. *et al.* Fault pattern and seismotectonic style of the Campania – Lucania 1980 earthquake (Mw 6.9, Southern Italy): New multidisciplinary constraints. *Front. Earth Sci.* **8**, 608063 (2021).
59. De Landro, G. *et al.* High-precision differential earthquake location in 3-D models: evidence for a rheological barrier controlling the microseismicity at the Irpinia fault zone in southern Apennines. *Geophys. J. Int.* **203**, 1821–1831 (2015).
60. Zaliapin, I., Gabrielov, A., Keilis-Borok, V. & Wong, H. Clustering analysis of seismicity and aftershock identification. *Phys. Rev. Lett.* **101**, 018501 (2008).
61. Sukan, M., Campanella, S., Chiaraluze, L., Michele, M. & Vuan, A. The unlocking process leading to the 2016 Central Italy seismic sequence. *Geophys. Res. Lett.* **50**, e2022GL101838 (2023).
62. Ogata, Y. & Katsura, K. Prospective foreshock forecast experiment during the last 17 years: Prospective foreshock forecast experiment. *Geophys. J. Int. no-no* <https://doi.org/10.1111/j.1365-246X.2012.05645.x> (2012).
63. Hainzl, S. & Fischer, T. Indications for a successively triggered rupture growth underlying the 2000 earthquake swarm in Vogtland/NW Bohemia. *J. Geophys. Res. Solid Earth* **107**, ESE-5 (2002).
64. Shapiro, K. L., Raymond, J. E. & Arnett, K. M. The attentional blink. *Trends Cogn. Sci.* **1**, 291–296 (1997).
65. Lucente, F. P. *et al.* Temporal variation of seismic velocity and anisotropy before the 2009 M W 6.3 LAquila earthquake Italy. *Geology* **38**, 1015–1018 (2010).
66. Chatelain, J. *Étude fine de la sismicité en zone de collision continentale à l'aide d'un réseau de stations portables: la région Hindu-Kush–Pamir* (Université Paul Sabatier, 1978).
67. De Natale, G., Crippa, B., Troise, C. & Pingue, F. Abruzzo, Italy, earthquakes of April 2009: Heterogeneous fault-slip models and stress transfer from accurate inversion of ENVISAT–InSAR Data. *Bull. Seismol. Soc. Am.* **101**, 2340–2354 (2011).
68. Peng, H. *et al.* MoDUO1, a Duo1-like gene, is required for full virulence of the rice blast fungus *Magnaporthe oryzae*. *Curr. Genet.* **57**, 409–420 (2011).
69. Parsons, T., Geist, E. L., Console, R. & Carluccio, R. Characteristic earthquake magnitude frequency distributions on faults calculated from consensus data in California. *J. Geophys. Res. Solid Earth* **123**, 10–761 (2018).
70. Gomberg, J. & Johnson, P. Dynamic triggering of earthquakes. *Nature* **437**, 830–830 (2005).
71. Calderoni, G., Rovelli, A., Ben-Zion, Y. & Di Giovambattista, R. Along-strike rupture directivity of earthquakes of the 2009 LAquila, central Italy, seismic sequence. *Geophys. J. Int.* **203**, 399–415 (2015).
72. Zambonelli, E., De Nardis, R., Filippi, L., Nicoletti, M. & Dolce, M. Performance of the Italian strong motion network during the 2009, LAquila seismic sequence (central Italy). *Bull. Earthq. Eng.* **9**, 39–65 (2011).
73. Barberio, M. D., Barbieri, M., Billi, A., Doglioni, C. & Petitta, M. Hydrogeochemical changes before and during the 2016 Amatrice–Norcia seismic sequence (central Italy). *Sci. Rep.* **7**, 11735 (2017).
74. Chiarabba, C., Buttinelli, M., Cattaneo, M. & De Gori, P. Large earthquakes driven by fluid overpressure: The apennines normal faulting system case. *Tectonics* **39**, e2019TC006014 (2020).
75. Chiodini, G. *et al.* Correlation between tectonic CO₂ Earth degassing and seismicity is revealed by a 10-year record in the Apennines. *Italy. Sci. Adv.* **6**, eabc938 (2020).
76. Gabrielli, S. *et al.* Scattering attenuation images of the control of thrusts and fluid overpressure on the 2016–2017 Central Italy seismic sequence. *Geophys. Res. Lett.* **50**, e2023GL103132 (2023).
77. Vuan, A., Sukan, M., Amati, G. & Kato, A. Improving the detection of low-magnitude seismicity preceding the Mw 6.3 LAquila earthquake: development of a scalable code based on the cross correlation of template earthquakes. *Bull. Seismol. Soc. Am.* **108**, 471–480 (2018).
78. Akinci, A., Munafò, I. & Malagnini, L. S-wave attenuation variation and its impact on ground motion amplitudes during 2016–2017 Central Italy earthquake sequence. *Front. Earth Sci.* **10**, 903955 (2022).
79. Ciotoli, G., Etioppe, G., Lombardi, S., Naso, G. & Tallini, M. Geological and soil-gas investigations for tectonic prospecting: preliminary results over the Val Roveto Fault (central Italy). *Geol. Romana* **29**, 483–493 (1993).
80. Miller, S. A. *et al.* Aftershocks driven by a high-pressure CO₂ source at depth. *Nature* **427**, 724–727 (2004).

81. Talone, D., De Siena, L., Lavecchia, G. & De Nardis, R. The attenuation and scattering signature of fluid reservoirs and tectonic interactions in the Central-Southern Apennines (Italy). *Geophys. Res. Lett.* <https://doi.org/10.1029/2023GL106074> (2023).
82. Walters, R. J. *et al.* Dual control of fault intersections on stop-start rupture in the 2016 Central Italy seismic sequence. *Earth Planet. Sci. Lett.* **500**, 1–14 (2018).
83. Chiaraluca, L., Valoroso, L., Piccinini, D., Di Stefano, R. & De Gori, P. The anatomy of the 2009 L'Aquila normal fault system (central Italy) imaged by high resolution foreshock and aftershock locations. *J. Geophys. Res.* **116**, B12311 (2011).
84. Sugan, M., Kato, A., Miyake, H., Nakagawa, S. & Vuan, A. The preparatory phase of the 2009 M_w 6.3 L'Aquila earthquake by improving the detection capability of low-magnitude foreshocks. *Geophys. Res. Lett.* **41**, 6137–6144 (2014).
85. Picozzi, M., Spallarossa, D., Iaccarino, A. G. & Bindi, D. Temporal evolution of radiated energy to seismic moment scaling during the preparatory phase of the M_w 6.1, 2009 L'Aquila earthquake (Italy). *Geophys. Res. Lett.* **49**, e2021GL097382 (2022).
86. Castaldo, R. *et al.* Coseismic stress and strain field changes investigation through 3-D finite element modeling of DInSAR and GPS measurements and geological/seismological data: The L'Aquila (Italy) 2009 earthquake case study. *J. Geophys. Res. Solid Earth* **123**, 4193–4222 (2018).
87. Sánchez-Reyes, H., Essing, D., Beaucé, E. & Poli, P. The imbricated foreshock and aftershock activities of the Balsorano (Italy) M_w 4.4 normal fault earthquake and implications for earthquake initiation. *Seismol. Res. Lett.* **92**, 1926–1936 (2021).
88. Ross, Z. E., Cochran, E. S., Trugman, D. T. & Smith, J. D. 3D fault architecture controls the dynamism of earthquake swarms. *Science* **368**(6497), 1357–1361 (2020).
89. Chiaraluca, L., Collettini, C., Cattaneo, M. & Monachesi, G. The shallow boreholes at The Altotiberina near fault observatory (TABOO; northern Apennines of Italy). *Sci. Drill.* **17**, 31–35 (2014).
90. Vuan, A. *et al.* Intermittent Slip along the alto Tiberina low-angle normal fault in Central Italy. *Geophys. Res. Lett.* **47**, e2020GL089039 (2020).
91. Vuan, A., Sugan, M., Chiaraluca, L. & Di Stefano, R. Loading rate variations along a midcrustal shear zone preceding the M_w 6.0 earthquake of 24 August 2016 in Central Italy. *Geophys. Res. Lett.* **44**, 12–170 (2017).
92. Baillard, C., Crawford, W. C., Ballu, V., Hibert, C. & Mangeny, A. An automatic kurtosis-based P- and S-phase picker designed for local seismic networks. *Bull. Seismol. Soc. Am.* **104**, 394–409 (2014).
93. Ross, Z. E., Trugman, D. T., Hauksson, E. & Shearer, P. M. Searching for hidden earthquakes in Southern California. *Science* **364**, 767–771 (2019).
94. Simon, V., Kraft, T., Diehl, T. & Tormann, T. Possible precursory slow-slip to Two M_L ~3 mainevents of the diemtigen micro-earthquake sequence. *Switzerland. Geophys. Res. Lett.* **48**, e2021GL093783 (2021).
95. Gardner, J. K. & Knopoff, L. Is the sequence of earthquakes in Southern California, with aftershocks removed, Poissonian?. *Bull. Seismol. Soc. Am.* **64**, 1363–1367 (1974).
96. Kagan, Y. Y. & Jackson, D. D. Long-term earthquake clustering. *Geophys. J. Int.* **104**, 117–134 (1991).
97. Goes, S. D. B. & Ward, S. N. Synthetic seismicity for the San Andreas fault. *Ann. Geofis.* **XXXVII**, 6 (1994).
98. Griffin, J. D., Stirling, M. W. & Wang, T. Periodicity and clustering in the long-term earthquake record. *Geophys. Res. Lett.* **47**, e2020GL089272 (2020).
99. Vidale, J. E. & Shearer, P. M. A survey of 71 earthquake bursts across southern California: Exploring the role of pore fluid pressure fluctuations and aseismic slip as drivers. *J. Geophys. Res. Solid Earth* **111**, 2005JB004034 (2006).
100. Munafò, I., Malagnini, L. & Chiaraluca, L. On the relationship between M_w and M_L for small earthquakes. *Bull. Seismol. Soc. Am.* **106**, 2402–2408 (2016).
101. Hanks, T. C. & Kanamori, H. A moment magnitude scale. *J. Geophys. Res. Solid Earth* **84**, 2348–2350 (1979).
102. Amezawa, Y., Maeda, T. & Kosuga, M. Migration diffusivity as a controlling factor in the duration of earthquake swarms. *Earth Planets Space* **73**, 148 (2021).

Acknowledgements

This research was supported by DiSPuTer Department funds (Rita de Nardis) and derives from a collaboration between CRUST (UR-Chieti) and OGS, established in 2020. ArcMap by ESRI, ArcMap/ArcGIS, v. 10.8. <https://www.esri.com/en-us/home> was used to generate the base map. The Generic Mapping Tool (GMT) was applied for some of the figures of this article; Move software (suite by Petroleum Experts, Petex at <https://www.petex.com/products/move-suite/>) for the 3D fault model reconstruction.

Author contributions

RdN: Conceptualization, Formal analysis, Investigation, Writing—Original draft preparation, Reviewing and Editing, Visualization; AV: Conceptualization, Formal analysis, Investigation, Writing, Original draft preparation, Reviewing and Editing; LC: data curation, Formal analysis, Investigation; DT: Formal analysis, Reviewing and Editing; MAR: Visualization, Review and Editing; GL: Investigation, Visualization, Writing.

Competing interests

The authors declare no competing interests.

Additional information

Supplementary Information The online version contains supplementary material available at <https://doi.org/10.1038/s41598-024-69118-8>.

Correspondence and requests for materials should be addressed to R.N.

Reprints and permissions information is available at www.nature.com/reprints.

Publisher's note Springer Nature remains neutral with regard to jurisdictional claims in published maps and institutional affiliations.

Open Access This article is licensed under a Creative Commons Attribution-NonCommercial-NoDerivatives 4.0 International License, which permits any non-commercial use, sharing, distribution and reproduction in any medium or format, as long as you give appropriate credit to the original author(s) and the source, provide a link to the Creative Commons licence, and indicate if you modified the licensed material. You do not have permission under this licence to share adapted material derived from this article or parts of it. The images or other third party material in this article are included in the article's Creative Commons licence, unless indicated otherwise in a credit line to the material. If material is not included in the article's Creative Commons licence and your intended use is not permitted by statutory regulation or exceeds the permitted use, you will need to obtain permission directly from the copyright holder. To view a copy of this licence, visit <http://creativecommons.org/licenses/by-nc-nd/4.0/>.

© The Author(s) 2024